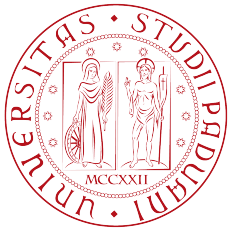

Università degli Studi di Padova

FACOLTÀ DI DI SCIENZE MATEMATICHE FISICHE E NATURALI
Corso di Laurea Magistrale in Fisica

Tesi di laurea magistrale

Design and optimization around 1 MeV of a calorimeter for a CubeSat mission

Candidato:
Francesco Berlato

Matricola 1093135

Relatore:
Prof. Denis Bastieri

Correlatore:
Dott. Riccardo Rando

Anno Accademico 2015–2016

Contents

Introduction

Gamma-ray astrophysics has obtained incredible scientific achievements in the last decade, mainly thanks to the great performance of the *Fermi Large Area Telescope*, and will continue to do so in the years to come with the new *Cherenkov Telescope Array*.
Those detectors are, however, designed to observe high or very high energy photons ($\gtrsim$100 MeV) in the gamma spectrum, which leaves the medium energies ($\sim$0.1-10 MeV) out of the effective range of the instruments.
This region of the spectrum, in its interaction with matter, is dominated by the Compton scattering, and only once has been studied by a dedicated instrument: the COMPTEL space telescope, which operated from the 1991 to the 2000.
Although there are other space telescopes which explore this energy range, such as SPI and IBIS on INTEGRAL, after COMPTEL there was no detector with a better sensitivity in the Compton region (we can see that, for example, in the plot at page 7).
This means that currently we have a 16 year gap from the last observations made in this range. Furthermore, COMPTEL's technology is much older than its launch date, dating back to the late '70 and early '80, making it obsolete by today standards.

As of today, there are mission proposals (such as ASTROGAM or COMPAIR) to cover such an important region of the gamma-ray spectrum, but none of them is yet approved, and in any case it would take them many years to be ready.
It is then evident the need for a new detector to succeed COMPTEL, and fill the gap left in the observations in the gamma spectrum by the major instruments until now.

Regarding the detector design we propose a pathfinder detector that, just by using today's technology, would already have a big advantage over COMPTEL, one for all the electron tracking capability. Furthermore the detector can retain very compact dimensions (using the CubeSat standard), making it easier and less expensive to both build and launch into orbit. Of course, using different instruments and materials, the new detector needs to be carefully designed and optimized. Such is the purpose of this thesis: to design and optimize this detector, and predict its performance by means of Monte Carlo simulations, with a particular focus on the calorimeter performance.

1 The current state of medium energy gamma-ray astronomy

Medium energy gamma-rays are roughly defined as the photons in the energy range of 1-30 MeV; in such energy range, there are various possible interactions of the photons with matter: while at lower energies, the total cross section is dominated by the photoelectric effect and at higher energies pair production becomes the most important component, here the greatest contribution is given by the Compton interaction, as we can see in figure Figure 1.1.

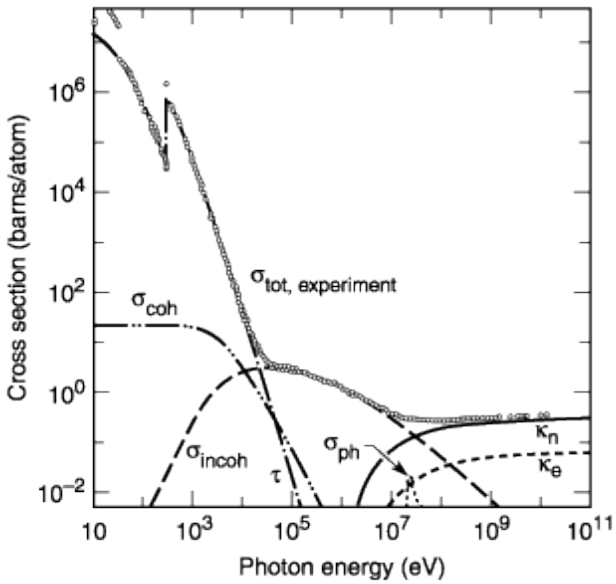

Figure 1.1: Carbon's photon cross section different contributes at increasing energy.

Before starting the discussion of the detector and its operating principles, it is important to understand what is the current status of gamma-ray astronomy, which, as we will see, motivates the need of a dedicated detector for medium energy gamma-rays.

1.1 Comptel

First of all, let us introduce COMPTEL, the last dedicated detector observing this energy range. This will allow us to understand what we can do better and what are the limits of a compact detector design like the one which will be discussed from chapter 4 onwards.
COMPTEL (*Imaging Compton Telescope*) was an imaging wide-field gamma-ray telescope, sensitive to photons between 800 keV and 30 MeV, with a field of view of $\sim$1.5 sr. It was one of the four detectors onboard the *Compton Gamma Ray Observatory*, a space mission which flew from 1991 to 2000.

It consisted of two detector arrays, the upper one was a liquid scintillator (low density), the lower one was instead made of NaI crystals (high density). The gamma-ray detection followed the coincidence of two consecutive interactions: the first detector served the purpose of Compton-scattering the incoming photon and measuring the electron's energy, while the second, lower one was meant to absorb the scatter photon. The location and energy of both interactions were measured.

The two detector layers were separated by a distance of 1.5 m from each other, allowing both a time-of-flight measurement between the two planes and an absolute time measurement for the two interactions. The necessary timing was possible because of the use of photo-multiplier tubes, allowing ns estimates. This represented a very big advantage during the event reconstruction sequence (especially with background rejection), at expense of a very big volume for the whole structure. The detector was entirely surrounded by an anti-coincidence shield of plastic scintillators (1.5 cm thick), which rejected the background events due to incoming charged particles. A schematic of the detector is in Figure 1.2.

The upper detector (D1 in figure) consisted of 7 cylindrical modules of liquid scintillator, each viewed by 8 photomultiplier tubes.
The lower detector (D2 in figure) consisted instead of 14 cylindrical NaI(Tl) crystals, each of them coupled to 7 photomultiplier tubes.

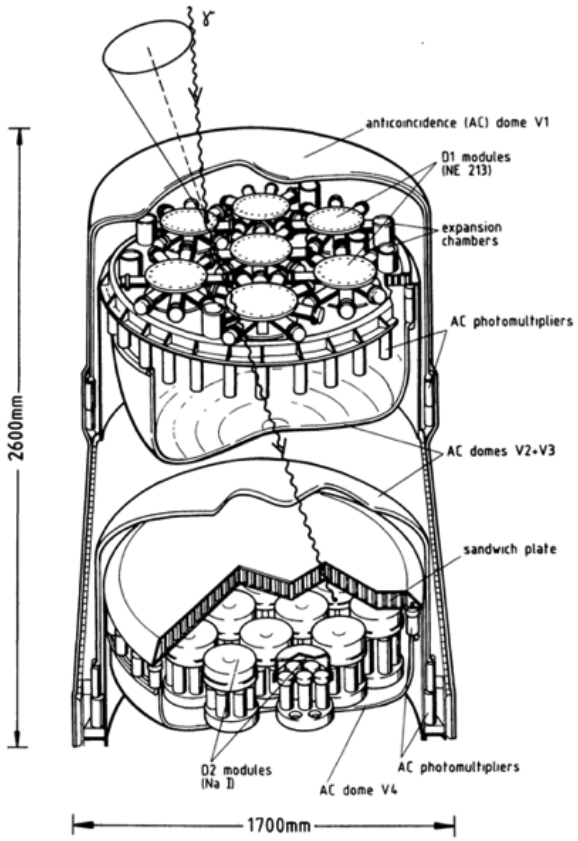

Figure 1.2: Schematic of COMPTEL.

In COMPTEL (and more generally, in a Compton telescope), the incoming photon has to interact in two independent sensitive parts of the detector to allow the reconstruction of the event.

The variables measured are the interaction positions X_1, X_2 and the energy depositions E_1, E_2 in each of the two detectors D1 and D2 (see Figure 1.3). Of course this is the optimal scenario: it is always possible that the energy of the scattered photon or the electron, or both, are underestimated due to the leakage of the energy lost in the calorimetric measurements.

The time of flight and its sign, that is the difference between the absolute times for the first and second detector, are extremely important to determine the general direction of the event (upwards or downwards), which is very useful for background rejection in the case of the Earth's albedo, which comes from the atmosphere.
As we will see in chapter 2, even without measuring the direction of the recoil electron we can infer an *event circle*, where the direction of the initial photon should be contained (assuming a precise measurement of the energy). With multiple Compton events from the same source, it is then possible to reconstruct $\vec{e}_i$, i.e. the source position[1].

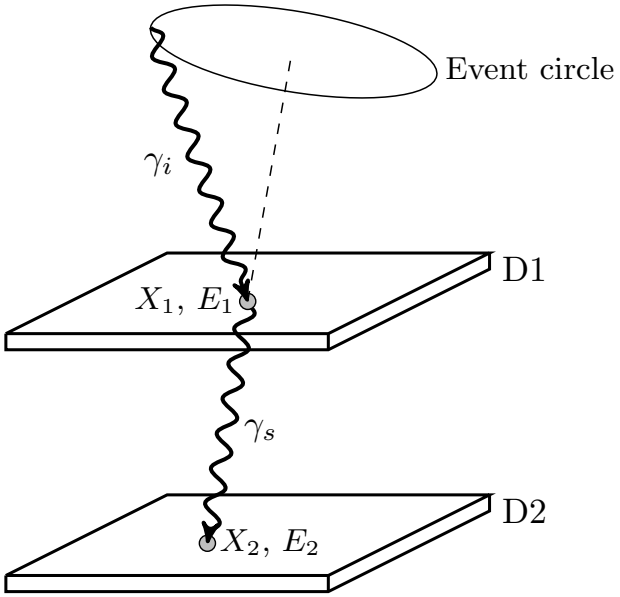

Figure 1.3: Example of COMPTEL-type interaction.

The total energy resolution (obtained from the *Full Width Half Maximum* of the total absorption peak) of the detector improve with increasing energy, ranging from about 10% at 1 MeV to 5% at 20 MeV. The spatial resolution (at $1\,\sigma$) at 1 MeV was approximately 2 cm for detector D1 and 1 cm for detector D2. These energy and space resolutions, after the event reconstruction process, result in an angular resolution of 1–2°, again a function of total energy and zenith angle[2].

[1] Here, I have omitted many of the complexities involved in the event reconstruction process. We will have the opportunity of seeing them in greater detail in chapter 2.

[2] Zenith angle here refers to the angle between the telescope pointing direction and the source position.

It is important to note that the Compton interaction of the initial photon in D1, with absorption of the scattered photon in D2, is only one of the many channels of the event reconstruction. For example, pair production is also a possibility for photons of high enough energy, with the additional complication that the pair (or the recoil electron for Compton) can emit bremsstrahlung photons, which can trigger the data acquisition by being absorbed in D2.

A useful parameter to quantify "how much" the detector can see, is the effective area, which is given by:

$$A_{eff}(\theta, \phi, E) = A_{geo}(\theta, \phi) \cdot \epsilon(\theta, \phi, E) \tag{1.1}$$

where A_{geo} is the geometrical area of the detector at a certain inclination with respect to the source and ϵ is the the efficiency of the detector at a certain zenith angle and energy of the incoming photons. In Figure 1.4 we can see a plot of COMPTEL effective area as function of the source's photon energy.

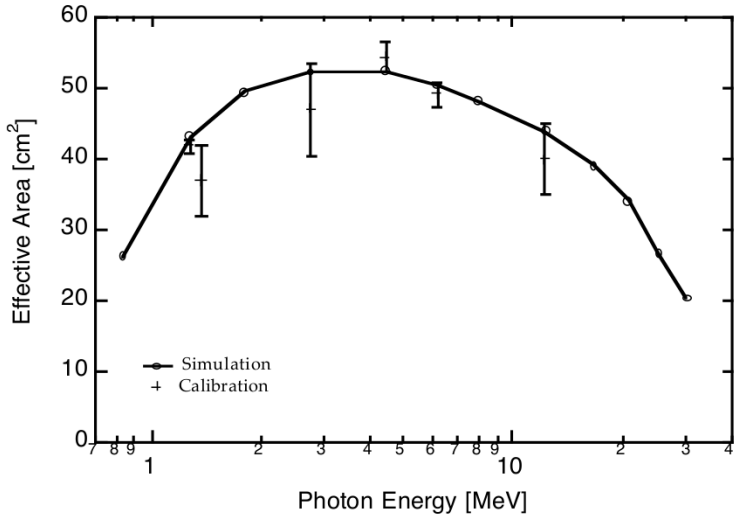

Figure 1.4: COMPTEL effective area as a function of the source's photons energy [9].

The effective area is also heavily dependent from the zenith angle, as we can see in Figure 1.5.

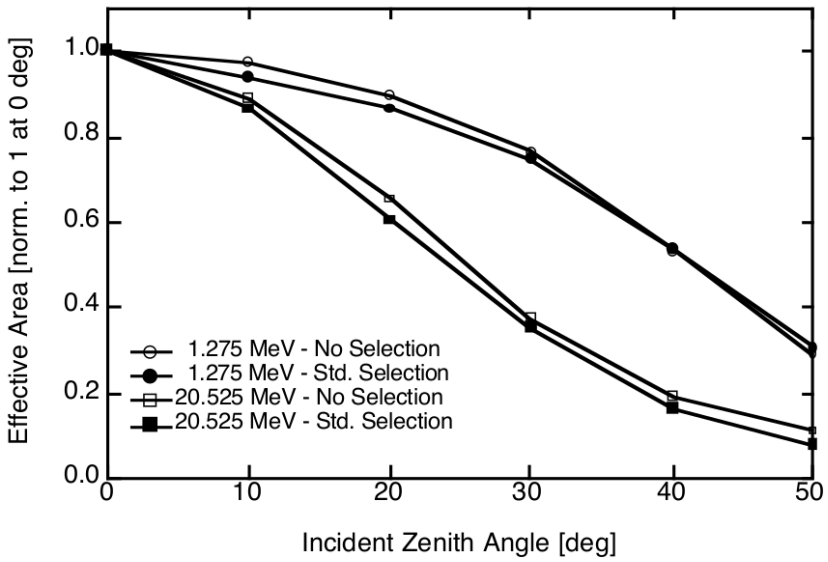

Figure 1.5: COMPTEL effective area as a function of the zenith angle.

An extremely important parameter for a space telescope is its sensitivity[3]. The sensitivity of a detector is the minimum flux which a source needs to have to be able to be distinguished from the background, with a given statistical significance. A more detailed explanation of how sensitivity is calculated for our detector will be provided in section 6.4.
The sensitivity photon flux is thus calculated, using Poisson's statistics, as in the following:

$$F_s = \frac{z\sqrt{N_{src} + N_{bkg}}}{T_{eff} A_{eff}} \tag{1.2}$$

where z is the number of Poisson's error bars (usually $z = 3$ or $z = 5$), N_{src} is the number of source counts, N_{bkg} is the number of background counts, both with an effective observation time T_{eff} and an effective area A_{eff}. Notice that T_{eff} is not the total observation time, as we have to take into account the dead time of the detector and source occultation.

[3]Here and for the rest of the thesis when discussing sensitivity we will implicitly refer to the continuum one. For a brief overview on the various sensitivity types of the detector, see section 6.4

This formula can easily be obtained if we remember that $N_{src} = F_s T_{eff} A_{eff}$ and imposing a certain statistical significance z. For more details on the sensitivity estimation for COMPTEL, see [8].
In Figure 1.6 we can see COMPTEL continuum sensitivity (i.e. with respect to a continuous spectral distribution), notice that, as of now, there have not been any instruments with better sensitivity in most of that energy range.

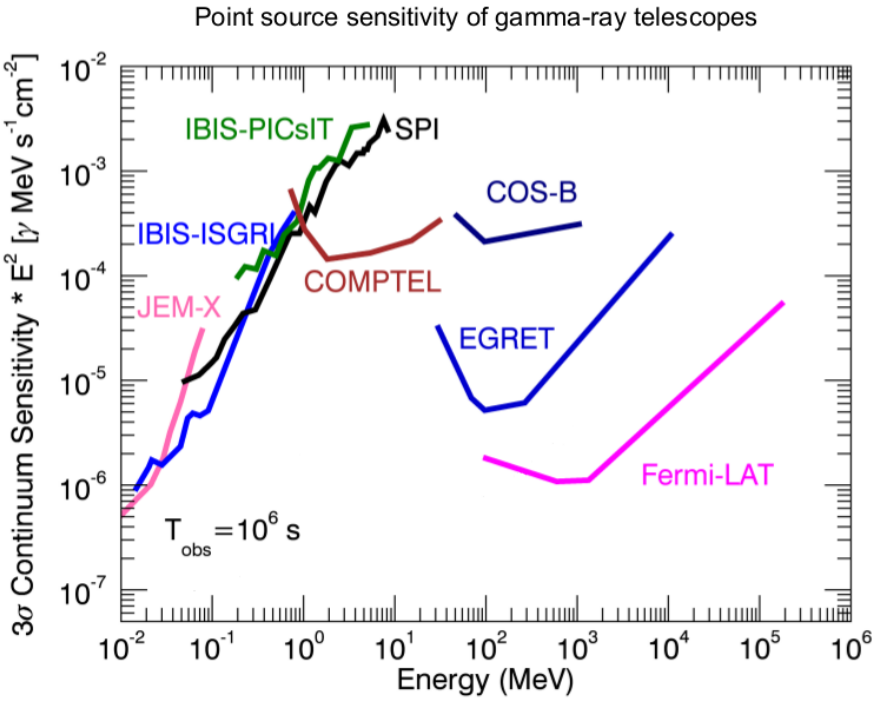

Figure 1.6: COMPTEL and other space telescopes continuum sensitivity.

For a more detailed description of COMPTEL and its instruments response, see [8].

1.2 Integral

As you can see from Figure 1.6, COMPTEL is not the only detector to have observed the medium energy range, although it still retains the best performance in this region of the spectrum.
Another space telescope worth mentioning is INTEGRAL (*INTErnational Gamma-Ray Astrophysics Laboratory*), launched in 2002 and still functioning as of today. The spacecraft (without solar panels) is roughly $3\times4\times5\,\mathrm{m}^3$, with a mass of $\sim$4000 kg, which make it a medium class space mission.

The space telescope observes photons with energies 15 keV $\lesssim E \lesssim$ 10 MeV and the scientific payload of our interest is composed by two different instruments:

- SPI, an extended gamma-ray spectrometer operating over energy the range 20 keV $\lesssim E \lesssim$ 8 MeV.
- IBIS, an extended gamma-ray imager operating over the energy range 15 keV $\lesssim E \lesssim$ 10 MeV.

We will focus on an overview of SPI (*SPectrometer on INTEGRAL*), which is overall the most performing instrument in the MeV region and thus the one we are most interested in.
SPI consists of an array of 19 Germanium detectors, each $6\times6\times7\,\mathrm{cm}^3$ big, all kept at a temperature of 80 K by a cooling system. The whole detector is than surrounded by a Bismuth germanate (BGO) veto system to reject charged background from cosmic rays. The imaging capabilities are obtained by placing a Tungsten coded aperture mask[4] at a distance of 1.7 m from the detector plane. The total mass of SPI is $\sim$1300 kg, again far from what could be defined a compact detector.
This design achieves a field of view of 16°, with an ARM, the *Angular Resolution Measurement* (see section 2.3), with a FWHM of 2.5° and a FWHM for the energy resolution at 1.33 MeV, of 3 keV; while Figure 1.6 the achieved continuum sensitivity can be seen. Note however that the region around 1 MeV has a worse sensitivity compared to the one from COMPTEL.

For more details on INTEGRAL and its scientific payload, see [6].

[4] In simplified way, a coded mask can be thought as a grid of elements which are either transparent or opaque to photons, thus limiting the possible directions for the detected photons. This greatly decreases the possible background, at the price of a much smaller field of view for the detector and a bigger weight and volume for the space telescope.

1.3 Fermi LAT

The *Fermi Large Area Telescope* (*Fermi* LAT), is a pair production space telescope, launched in 2008 and still operational. While this instrument is designed for higher energy gamma-rays ($\gtrsim$100 MeV), it is still worth a quick overview, since its basic structure (a Silicon tracker plus a crystal calorimeter) has proven to be quite effective and reliable, and is the basis of modern Compton telescopes.

For the LAT, both the tracker and the calorimeter are structured in a 4×4 grid of smaller units. Each tracker module is made of 19 trays of single-sided Silicon Strip Detectors (SSD), each shifted in orientation by 90° with regards to the previous one, allowing thus the tracking in both x and y direction, assuming that the planes are stacked along the z-axis. Additionally, between the trays, Tungsten foils are inserted to provide the cross section needed for the photon to be able to produce the pairs. Each SSD is $8.95\times8.95\,\mathrm{cm}^2$ wide and 400 µm thick, with a pitch for the strips of 228 µm, which allows an excellent tracking capability for the e^+e^-.

As for the calorimeter, each module is made of 8 layers of 12 crystals, for a total of 96 CsI(Tl) crystals, each $2.7\times2.0\times32.6\,\mathrm{cm}^3$ big. The layers are then placed in a hodoscopic[5] configuration. The number of the crystals and their sizes are a compromise between their ability to fully absorb the photons (bigger crystals), their ability of reconstructing the electronic shower position (more numerous crystals) and the electronic noise introduced by the read-outs (obviously increasing with the number of crystals).

The instrument is also enclosed in anti-coincidence detector (ACD) to prevent the charged radiation from triggering data acquisition. This is done by using a plastic scintillator, which uses a veto system to prevent the data acquisition whenever a charged particle enters the instrument. With this, an average efficiency of 99.97% of charged background rejection is achieved.

For a detailed explanation on the Fermi LAT scientific payload and performance refer to [5].

[5] An hodoscopic configuration is obtained by laying the long direction of the crystals along the xy plane, alternating the direction along x and y in consecutive planes.

1.4 Future missions

Aside from the current and past missions, there are plans for new space telescopes in the future (in ∼10 yr or more). Although none of them has yet been definitively approved, there are currently two medium class missions proposals under evaluation, ASTROGAM and COMPAIR.

1.4.1 Astrogam

ASTROGAM (the merging of the two previously different proposals ASTROMEV and GAMMA-LIGHT) is a medium class space telescope proposed by the European Space Agency (ESA) in 2015. The energy range for its observation is mainly 0.3-100 MeV, but the instrument is also capable of extending it to the GeV scale. The sensitivity for the main range is expected to be at least 10 times better then the best previous observations. The telescope features a very large field of view of 2.5 sr, coupled with a high angular resolution, especially at higher energies (0.15° at 1 GeV). It features both Compton and pair detection capabilities, although the priority is given to the Compton events.

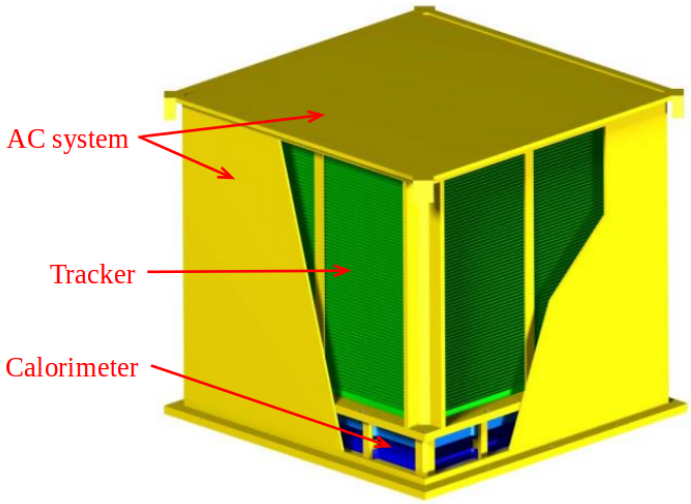

Figure 1.7: Schematic of ASTROGAM design.

As visible in Figure 1.7, ASTROGAM features a setup similar to the *Fermi* LAT, with a tracker made of 70 trays of double-sided Silicon strip (DSSD) detectors. Each tracker plane is assembled as a 6×6 grid of such detectors, each 9.5×9.5 cm^2 wide, with a thickness 400 µm and a pitch for the strips of

400 µm. The spacing between each tray and the consecutive one is instead of 7.5 mm. Differently from the *Fermi* LAT, being Compton detection the main purpose of the instrument, there are no high Z material planes in between the tracker trays, since they would hinder the tracking of low energy electrons.

The calorimeter is made of 12544 bars of $5\times5\times50\,\mathrm{mm}^3$ big CsI(Tl) crystals, where the thickness of 5 cm corresponds to 2.7 radiation lengths[6]. The readout of each crystal is provided by Silicon drift detectors at both ends of the bar, which also allow the estimation of the position of interaction along the crystal and results in a spatial resolution of 5 mm. The overall calorimeter energy resolution is instead 4.5% at 662 keV.

ASTROGAM will also be capable of detecting the polarization of the source's photons. Finally, alike *Fermi* LAT, the detector is enclosed in a anticoincidence detector, made of plastic scintillators ∼5 mm thick. The charged background rejection reaches an efficiency of >99.99%.

For a more complete overview on ASTROGAM design and expected performance, refer to [4].

1.4.2 Compair

The *Compton-Pair Production Space Telescope* (COMPAIR) is based on a design similar to ASTROGAM, since it uses again a Silicon tracker and a calorimeter of scintillation material. The tracker is also made by DSSD detectors. In this case, there are 50 trays, each of which is a 5×5 grid of $9.5\times9.5\,\mathrm{cm}^2$ wide elements, with a thickness of 500 µm and a pitch of 250 µm. Overall, the tracker is similar to the one designed for ASTROGAM.

The difference between the two space telescopes lies mainly in the calorimeter setup, since it uses a combination of two different materials, as we can see from Figure 1.8. The upper calorimeter, in which the tracker is encased, is made of CZT (Cadmium Zinc Telluride). Under that, a second calorimeter made of CsI(Tl) is placed. The total thickness of the bottom calorimeter is ∼4.5 radiation lengths.

[6] The radiation length of a material is the mean path length required to reduce the energy of a relativistic charged particle by the factor 1/e as they pass through matter.

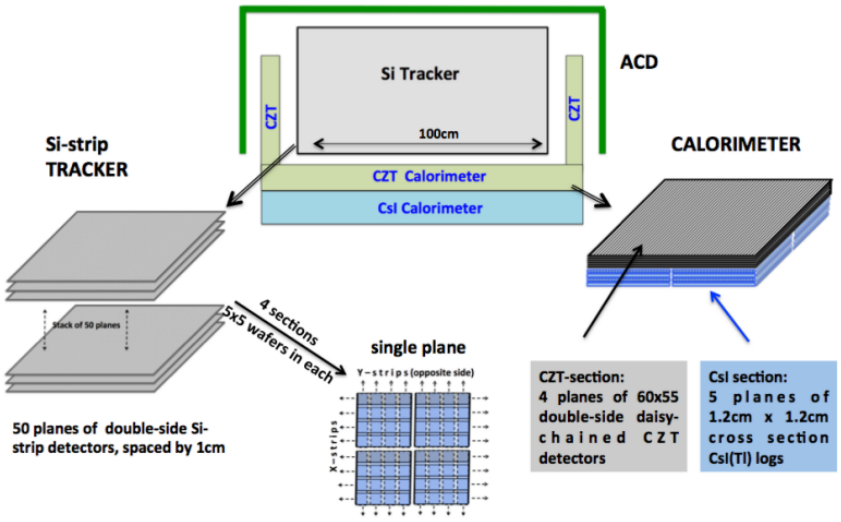

Figure 1.8: Schematic of COMPAIR design.

The CZT calorimeters are made of 4 stacked planes, each a grid of 25×25 double-sided CZT strip detectors, $2\times2\times0.5\,\mathrm{cm}^3$ big. The CsI(Tl) calorimeter is instead made of $1.2\times1.2\times32\,\mathrm{cm}^3$ crystals, read by a Silicon photomultiplier on both ends. There are five planes of such crystals, placed in a hodoscopic configuration.
There is of course an ACD, with similar performance to the one designed for ASTROGAM.

For further details on COMPAIR, see [3].

1.4.3 A detector with compact design

Both ASTROGAM and COMPAIR are designed as medium class missions, meaning that the space telescopes will roughly be ten times smaller than the Fermi LAT. This means that whichever mission will end up being approved, it will require very long preparation times, and also an high budget ($\sim$ 500 million euro).
In this thesis, however, we will explore another possibility: designing a compact detector (see chapter 4 for more detailed specifics) which can potentially be launched very quickly and with much smaller expenses, while still retaining an overall performance superior or at least similar to that of COMPTEL.

2 Compton interaction

The Compton interaction, discovered in the 1923 by Arthur H. Compton, consists in the scattering of a photon by an electron. A schematic drawing of the Compton interaction is shown in Figure 2.1.
This process, which can easily be described by special relativity kinematics, is much more complicated in the realistic case of a detector, where we have to take into account measurement uncertainties, background events, wrong or incomplete reconstruction of the sequence etc. For this section of the thesis we will mainly refer to [13].
First of all, let us briefly summarize the Compton interaction from an "ideal" analytical standpoint, where the electron is at rest and we do not have to worry about any measurement issue. We will discuss the Compton interaction from an experimental point of view in section 2.2.

2.1 Compton kinematics

To compute the quantities we will need to reconstruct the initial photon direction and energy, we will thus make use of the conservation of energy and momentum:

$$E_i + E_0 = E_g + E_e \tag{2.1a}$$
$$\vec{p_i} = \vec{p_g} + \vec{p_e} \tag{2.1b}$$

where, as usual, E defines energies and p the momenta, with the subscript "i" for the incoming photon, "e" for the recoil electron and "g" for the scattered photon, while E_0 is the mass energy of the electron.

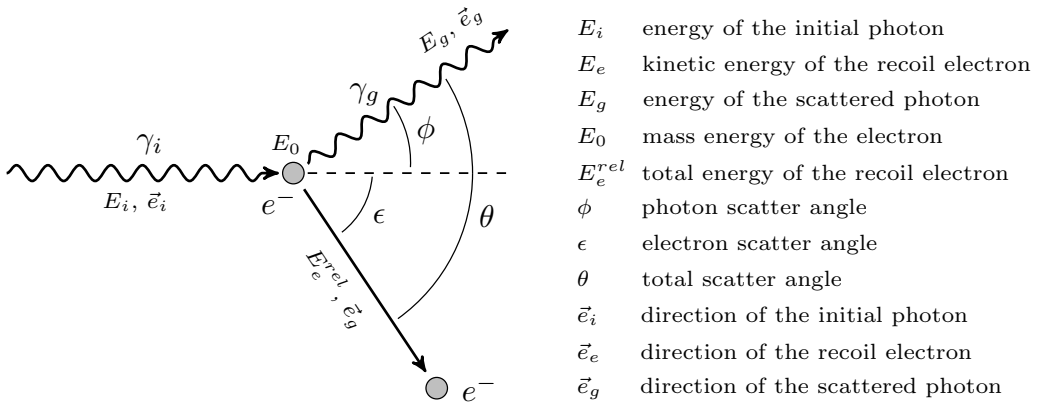

Figure 2.1: Compton scattering schematic.

Using $E_e^{rel} = \sqrt{E_0^2 + p_e^2 c^2}$ and $E_{i,g} = p_{i,g} c$, with c speed of light in the vacuum, we can compute the photon scatter angle ϕ:

$$\cos\phi = 1 - \frac{E_0}{E_g} + \frac{E_0}{E_g + E_e} \tag{2.2}$$

where the fact that ϕ can only assume values between 0° and 180° imposes the following restrictions on the scattered photon energy:

$$\frac{E_0 E_i}{2E_i + E_0} < E_g < E_i \tag{2.3a}$$

$$0 < E_g < \frac{2E_i^2}{2E_i + E_0} \tag{2.3b}$$

Furthermore, the calculations for the electron scatter angle ϵ and total scatter angle θ yield the following:

$$\cos\epsilon = \frac{E_e(E_i + E_0)}{E_i\sqrt{E_e^2 + 2E_e E_0}} \tag{2.4a}$$

$$\cos\theta = \frac{E_e(E_g - E_0)}{E_g\sqrt{E_e^2 + 2E_e E_0}} \tag{2.4b}$$

We can also calculate the direction of the incoming photon, which is:

$$\vec{e}_i = \frac{\sqrt{E_e^2 + 2E_e E_0}\cdot\vec{e}_e + E_g\vec{e}_g}{E_e + E_g} \tag{2.5}$$

From this analytical "ideal" standpoint it is always possible to reconstruct both the direction and the energy of the initial photon. In section 2.2 will see how this changes when measurement uncertainties or energy leakage are assumed.

2.1.1 Compton cross section

The differential cross section for Compton interaction has been calculated by Klein and Nishina (1929) and, for an unpolarized photon and free electron, is:

$$\left(\frac{d\sigma}{d\Omega}\right)_{free,unpol} = \frac{r_e^2}{2}\left(\frac{E_g}{E_i}\right)^2\left(\frac{E_g}{E_i} + \frac{E_i}{E_g} - \sin^2\phi\right) \tag{2.6}$$

where r_e is the classical radius of the electron[1]. From Figure 2.2 we can see that the differential cross section highly favors forward scattered photons at higher energies.

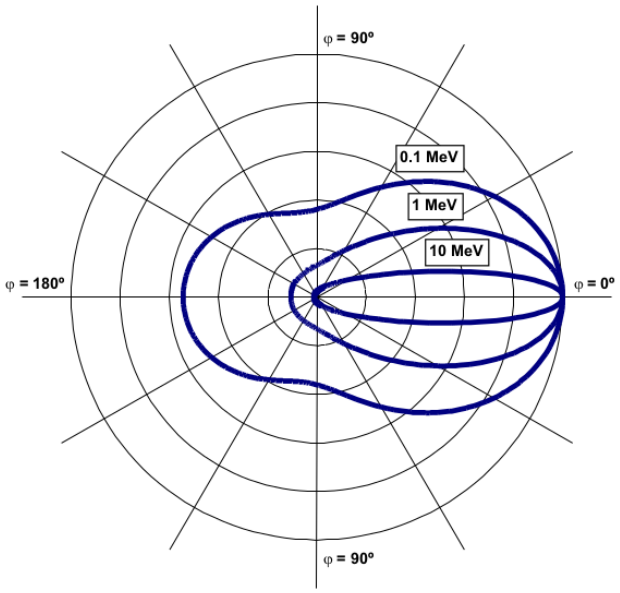

Figure 2.2: Klein-Nishina cross section in function of E_i and ϕ.

[1]Which, written explicitly, is $r_e = \frac{e^2}{4\pi\epsilon_0 E_0}$ with e elementary charge and ϵ_0 electrical permittivity of the vacuum.

It is also possible to compute the cross section in the case the photon is polarized, which is:

$$\left(\frac{d\sigma}{d\Omega}\right)_{free,pol} = \frac{r_e^2}{2}\left(\frac{E_g}{E_i}\right)^2\left(\frac{E_g}{E_i} + \frac{E_i}{E_g} - 2\sin^2\phi\cos^2\chi\right) \tag{2.7}$$

where χ is the azimuthal or polar scatter angle, which is the angle between the polarization vector of the incoming photon and the scatter plane. With this we can, at least in principle, reconstruct the polarization of a source.

2.2 Compton interaction in a detector

Everything seen until now is, of course, the "ideal" scenario. In a real Compton interaction in a detector, measurement uncertainties, missing quantities reconstructions and background events are sure to be expected.
For now, let us focus our attention on the first two problems, leaving the background discussion to chapter 6.

2.2.1 Missing direction measurement

Suppose that the detector was able to measure all of the energies, but was not able to measure both $\vec{e}_g$ and $\vec{e}_e$. For example, let's suppose that the measurement of the direction of the recoil electron is missing (as was the case for all COMPTEL's events). If we choose our reference frame so that its z-axis is parallel to the direction of the scattered photon, we have that:

$$\cos\phi = \vec{e}_i \circ \vec{e}_g = e_i^z \cdot e_g^z = e_g^z \tag{2.8}$$

since $||\vec{e}|| = 1$ for all the direction vectors and $e_g^z = 1$. From this, it immediately follows that:

$$(e_g^x)^2 + (e_g^y)^2 = 1 - \cos^2\phi = \sin^2\phi \tag{2.9}$$

For a fixed (i.e. measured) ϕ, this equation describes a circle, called *event circle*.
We can reparametrize it with $e_g^x = r\sin t$ and $e_g^y = r\cos t$, where $r = \sin\phi$.

$$\vec{e}_i = \begin{pmatrix} \sin\phi\sin t \\ \sin\phi\cos t \\ \cos\phi \end{pmatrix},\ t \in [0, 2\pi] \tag{2.10}$$

The event circle defines a cone with opening angle ϕ, which is called *Compton cone*. Obviously, with a single Compton event, it is not possible to reconstruct the direction of the initial photon, but we do know that its direction vector lies on the surface defined by the Compton cone. With multiple events, however, we can actually obtain this information from the intersection of the event circles.

In the same way as just done, it is possible to repeat the procedure for the case where $\vec{e}_e$ is known, but $\vec{e}_g$ is not. Assuming that this time we have chosen our reference frame to have the z-axis aligned with the direction of the recoil electron, we obtain:

$$\vec{e}_i = \begin{pmatrix} \sin\epsilon \sin t \\ \sin\epsilon \cos t \\ \cos\epsilon \end{pmatrix}, \; t \in [0, 2\pi] \tag{2.11}$$

Once again we have an event circle and a Compton cone, but this time with opening angle ϵ.

Lastly, note that so far we did not consider measurement uncertainties in our calculations. If we include their contributions, we have that the Compton cone develops a *thicker* surface. This, of course, is an additional complication to our event reconstruction, but does not compromise the validity of the procedure presented so far.

2.2.2 Missing energy measurements and energy leakage

In the case we have both direction measurements, but only one complete energy measurement is known, in principle it is possible to recover the missing energy using Equation 2.5. The problem with this, however, is that we do not know if there was any leakage, thus such approach is not applicable.
If we have an event of which both $\vec{e}_g$ and $\vec{e}_e$ are known, but E_g and E_e are unknown (or they measurements are incomplete), we can still retrieve some partial information on $\vec{e}_i$. Indeed, thanks to momentum conservation, we do know that $\vec{e}_i$ must lie in the same plane defined by $\vec{e}_g$ and $\vec{e}_e$. More precisely, the initial photon direction will lie between the angle defined by the inverse direction of the scattered photon and the inverse direction of the recoil electron (see Figure 2.3).

In the case we have at least partial energy measurements, we can further restrict the angle in which $\vec{e_i}$ lies. In fact, using spherical coordinates, we have that the initial photon direction lies in an arc of circle defined by

$$\vec{e_i} = ||(1-t)\vec{e_g} + t\vec{e_e}||, \quad t \in \left[\frac{\phi_{min}}{\theta}, \frac{\phi_{max}}{\theta}\right] \tag{2.12}$$

where ϕ_{min} and ϕ_{max} are computed from the partial energy measurements. Using our knowledge of the value of θ, we can use Equation 2.5 to obtain a relation between E_g and E_i, using quantities we know the value of:

$$E_e = \frac{2E_0E_g^2\cos^2\theta}{(E_g - E_0)^2 - E_g^2\cos^2\theta} \tag{2.13}$$

Thus, even without a complete set of measurements for our event, we can still obtain some kind of information on the source position.

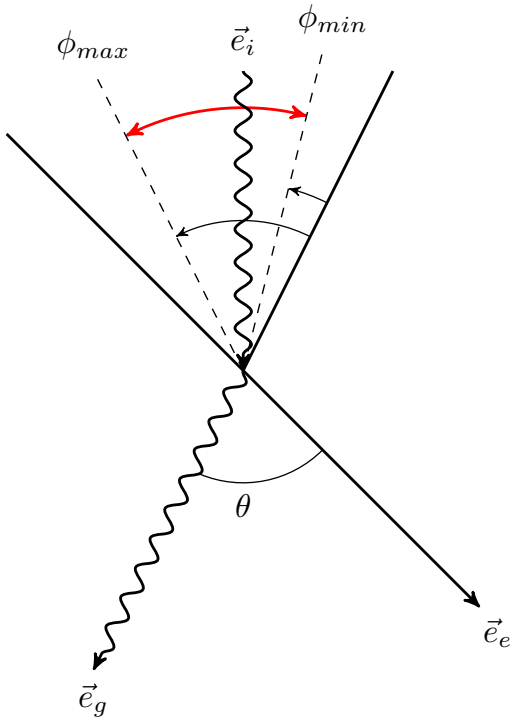

Figure 2.3: Schematic of a incomplete measurement. The range of possible values of $\vec{e_i}$ is marked in red.

2.2.3 Bound electron and Doppler broadening

In subsection 2.1.1 we made the assumption of having a still, unbound electron. If we release this constraint, we have to deal with an electron bounded to a nucleus, which implies that the particle is moving during the Compton interaction. In such conditions, the cross section is, obviously, different, and has been calculated by *Ribberfors and Berggren* (1982). Its expression is:

$$\left(\frac{d\sigma}{d\Omega}\right)_{bound} = \left(\frac{d\sigma}{d\Omega}\right)_{free} S_i(E_i, \phi, Z) \tag{2.14}$$

where S_i is called *incoherent scattering function* of the i-th shell electron, with Z atomic number of the scatter material.
Its differences compared to Klein-Nishina are, however, very small at energies greater than $E \gtrsim 100$ keV, as we can see in Figure 2.4.
Thus, since this is a minor issue in our energy range (at least, compared to the others), It will not be discussed in greater detail. Its effect, if not negligible, would be the worsening of the angular resolution of the detector. For further details, refer to [13].

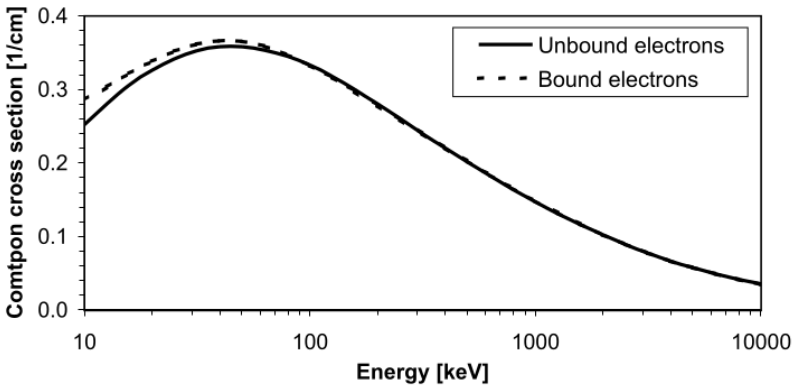

Figure 2.4: Bound cross section for Compton interaction.

2.3 Measures of angular resolution

While estimating the energy resolution of a Compton detector is usually a very simple matter (see chapter 6, for example), obtaining its angular resolution requires a bit more of attention. For an electron tracking telescope, which is our case, there are two angular resolutions to take into account.

The first, called ARM (*Angular Resolution Measure*), is defined as the smallest angular distance between the known (from simulation or calibration in laboratory) origin of the photon and the Compton cone; it is a measure of the thickness of the Compton scatter cone or arc. If the real initial direction of the photon lies within the cone, it mostly implies that the scattered gamma-ray was not completely absorbed, which yields a negative ARM value. On the other hand, an origin lying outside the cone usually means that the recoil electron was not completely absorbed, which implies a positive ARM value. Written explicitly, the ARM is obtained from the following:

$$\Delta\phi_{ARM} = \arccos(\vec{e}_i \circ \vec{e}_g) - \phi \tag{2.15}$$

where ϕ is the known "real" angle, either from simulation or calibration. If we have many events, each with its ARM value, we obtain a distribution which can be used to characterize the detector angular resolution, as we will see in chapter 5.

It is possible to do the same for the recoil electron (but only for tracked events), obtaining:

$$\Delta\epsilon_{ARM} = \arccos(\vec{e}_i \circ \vec{e}_e) - \epsilon \tag{2.16}$$

with ϵ "real" scatter angle of the electron. Photon and electron ARM, although useful estimations of the capabilities of the detector, have the problem of not taking into account both the scattered photon and recoil electron at the same time, and do not provide a definitive unique value capable of estimating how well the detector can reconstruct tracked events.
To solve this issue, we can use the *Scatter Plane Deviation* (SPD), defined as angle between the true scatter plane obtained from $\vec{e}_i$ and $\vec{e}_g$ (assuming a correct measure[2] of $\vec{e}_g$). Explicitly, this is written as:

$$\Delta\nu_{ARM} = \arccos((\vec{e}_g \times \vec{e}_i) \circ (\vec{e}_g \times \vec{e}_e)) \tag{2.17}$$

which can be used as a parameter to estimate the angular resolution of the detector for the tracked events.

As a final note, when talking about ARM in the following chapters, we will always refer to the photon ARM, which is defined for all Compton events, and hence is good parameter to check if the angular resolution improves when we modify the detector's design or use some kind of event selection.

[2]The reason for assuming a correct measure of $\vec{e}_g$ is that its estimation is a lot more reliable and easier then the estimation of $\vec{e}_e$.

3 Scientific objectives

Observing sources in the gamma-ray medium energy range, both galactic and extragalactic, is of fundamental importance for understanding the mechanisms responsible for the emission, and thus the inner workings of the sources themselves. From chapter 1, however, it should be clear that right now the best data we have is still the one from COMPTEL observations.
While the quantity and quality of observations at higher and lower energy have improved greatly in the last decade or so, this "gap" in the medium energy range is now hindering the advancement in the understanding of the emission models for many astrophysical sources. We provide an example in the next section.

3.1 The case of Markarian 421

Markarian 421 (Mrk 421) is an *Active Galactic Nucleus* (AGN), which is a compact region of a galaxy where the energy emission is much higher compared to that of normal stellar or interstellar processes. This is possible thanks to the interaction between the supermassive black hole inside the AGN and the accretion disk near it.
The black hole generates extremely strong magnetic fields, capable of accelerating particles (mainly protons and electrons) to energies of the TeV scale, or even higher. This is particularly visible when relativistic jets, which are jets of collimated plasma emitted in opposite direction from the object, are released. A schematic drawing of an AGN structure is visible in Figure 3.1.

Mrk 421 is a particular interesting object, being one of the closest AGNs, with a redshift of $z \sim 0.03$, and also a very bright gamma-ray source.
Mrk 421 is classified as a *blazar*, which, in the context of the AGNs unifying model (see [12], for example), is a source which relativistic jets are pointed within a small angle from the observer's line of sight.

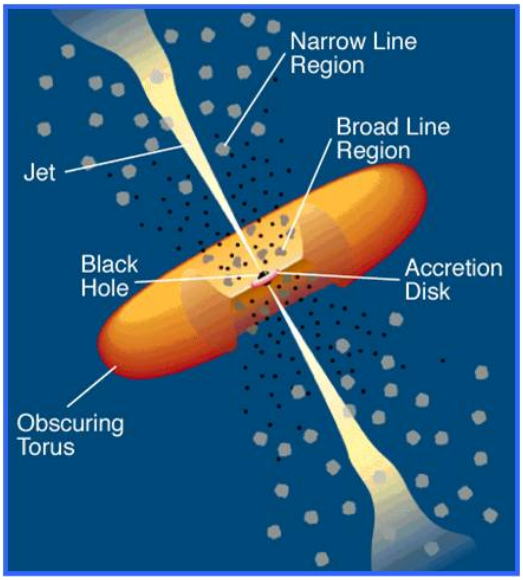

Figure 3.1: AGN schematic drawing.

Being discovered in 1992, well before the launch of the *Fermi* LAT, this source has been observed for a long time, and by a multitude of different instruments, as can be seen in Figure 3.2.
As you can see in the *Spectral Energy Distribution* (SED) plot, there is a big gap in the observations in the MeV region. This lack of data is of critical importance when studying the emission models for the source.

There are two main mechanisms of radiation emission for AGNs: the leptonic emission model (LEM) and the hadronic emission model (HEM). To briefly summarize the differences between the two, the LEM is reliant on the inverse Compton effect of the electrons, while the HEM model is more complex, since it involves both proton-proton and proton-photon interactions. The latter one, in particular, is thought to be more important at higher energies.
In an actual source, they are most likely both present, although which component is dominant at each energy is something that probably depends from case to case, and this is where the problem lies. Without data from the MeV region, where the two models are better discriminated, we are not able to determine how much is hadronic emission and how much is leptonic emission, which is limiting our ability of understanding what is really happening in the source. Observations in the medium energy range are thus needed.

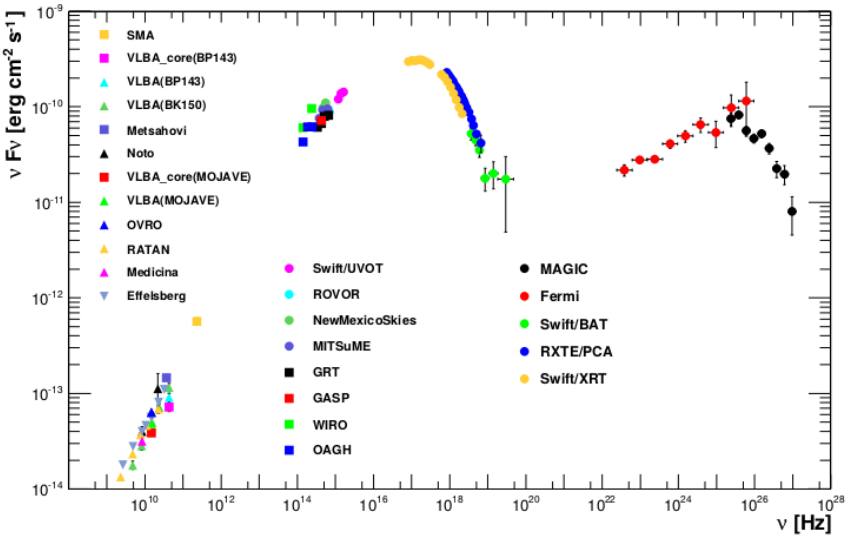

Figure 3.2: Markarian 421 SED [1]. Roughly, 1 MeV corresponds to $2 \cdot 10^{22}$ Hz.

3.2 Other scientific objectives

Of course, AGNs are not the only sources we can expect to observe in the medium energy range. Observation in the MeV region can potentially provide further insight on many aspects of astrophysical and cosmological interest, which are briefly summarized here:

- Relativistic jets: observations in the MeV range can provide crucial information for the models necessary to explain how the transition from the black hole's accretion disk to relativistic jet occurs.
- Estimation of the cosmic ray density in our galaxy in the MeV region.
- Radioactive nuclei emission line: in the MeV range there are many important emission lines of astrophysical interest, which can provide further information of the inner workings in star formation regions and supernovae.
- Observation of the Galactic Center: there is still much to understand regarding the Milky Way central region and the observations in the MeV range would be extremely useful.

- Investigating the extragalactic background in the MeV region: while at higher energy the *Fermi* LAT provided a lot of new data, in the MeV region there is a great lack of observations.
- Study of the populations of high energy AGNs at high redshift.
- Polarization studies: since the Compton cross section is polarization dependent, with enough statistics it is possible to reconstruct the source's photons polarization, providing further insight on the source emission mechanisms.
- Possible new mechanisms of acceleration in the MeV range: eventual discoveries in this field would be of particular benefit for the understanding of pulsars and magnetars emission at lower energies.
- Investigation of the solar flares acceleration mechanisms.
- Investigation of possible correlations in gravitational waves/neutrino emission and MeV range emission: with the recent successes in the observation of the gravitational waves, the next generation of gravitational interferometers will be able to observe a lot more of sources, thus the importance of having electromagnetic observations to study the correlations between the two kinds of emissions.

4 Detector basic design

Having now a good idea of the physics behind Compton detection and understanding what the detector needs to be able to do, we can start discussing its design in detail. However, before focusing on the performance of the scientific instruments onboard the space telescope, let us briefly summarize the satellite requirements and the tools used for the data analysis.

4.1 Satellite requirements

The satellite meant to host the space telescope is a *CubeSat*, which is a standardized model of nanosatellite. Each CubeSat is a cube of $10 \times 10 \times 10$ cm^3, but multiple CubeSats can be joined together to obtain a single bigger satellite. The space telescope is thus composed of one or multiple CubeSat modules, each identical in its volume and weight limits. The detector design in the following chapters is meant to satisfy a double unit satellite requirements, however such design can easily be extended to the case of a space telescope of multiple units.

Aside from weight and volume restrictions, one must also carefully consider the choice of the orbit. In principle, a satellite could be launched to fly either in a *Low Earth Orbit* (LEO) or in a *High Earth Orbit* (HEO)[1], but there are many technical difficulties in launching a nanosatellite in a HEO. Furthermore, as explained in subsection 6.3.1, background due to the activation of the satellite materials constitutes a major problem with this type of orbit. Hence, the only possible orbit for this CubeSat is a LEO.

[1] A LEO has an altitude of at least 160 km (where the orbital period is ∼90 min), while a HEO is placed much higher, with an orbital period >24 h.

4.2 The MEGAlib tools

The actual design and simulation work were done using MEGAlib (*Medium-Energy Gamma-ray Astronomy library*), developed by Andreas Zoglauer (see [2] and [7] for an overview of MEGAlib).
MEGAlib includes various packages, each one meant for a different step of the simulation and data analysis procedure:

1. Using *Geomega*, the detector geometry and materials are defined in a geometry file.
2. A source is chosen and then simulated with the detector response through *Cosima*, producing an output file with all simulated events.
3. From the previous output file, the measured events are reconstructed using *Revan*, producing a new output file.
4. The reconstructed events are then analyzed through *Mimrec*.

Also, to adapt the analysis to the needs of the thesis work, several additions written in C++ and Python have been used (allowing a detailed analysis using ROOT and PyROOT respectively).

4.3 Detector basic design

Having now all the background knowledge required, it is finally possible to start discussing the scientific instruments of the detector.
The detector fundamental design can be summarized in two main parts:

- A tracker unit on the upper half of the detector, made of a series of double-sided Silicon strip (DSSD) detectors planes stacked along the z-axis. Its main purpose is tracking the recoil electron from the Compton interaction, thus giving us the possibility of having a reconstructed direction even with a single (tracked) event. This is a capability that COMPTEL did not possess, and is an important step forward in the detector overall performance.
- A calorimeter unit in the lower half of the detector, made of a grid of CsI(Tl) crystals, which serves the purpose of measuring the energy and the direction of the scattered photon. Each crystal is read by two photodiodes at the extremities of the crystal, which also provide a measure of the position of interaction through the asymmetry of the light collected by the read-outs.

An example of such design is visible in Figure 4.1. The choice of using a Silicon tracker and CsI(Tl) calorimeter is mainly motivated by the reliability and good performance of such technologies, as the *Fermi* LAT demonstrated. Furthermore, this setup allows a compact design of the detector, without adding excessive weight to the CubeSat.

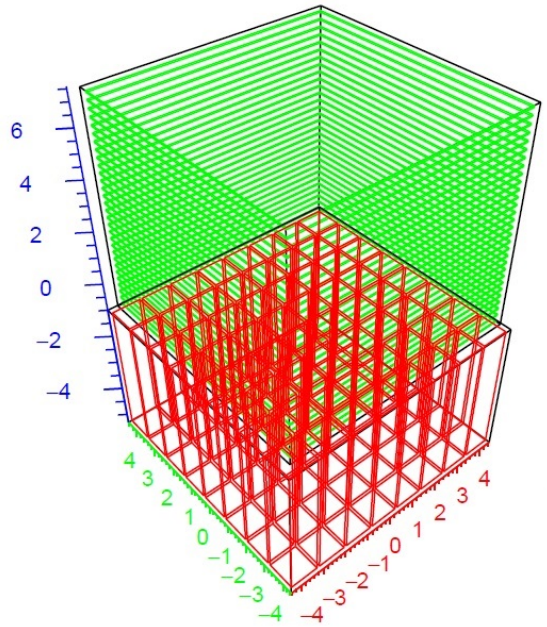

Figure 4.1: One of the initial designs of the detector.

From this basic setup, the detector design was improved and optimized, as will be explained in detail in chapter 5. Additionally, a lightweight ACD made of plastic scintillators can easily be added to the design to prevent nearly all (∼99.99%) of the charged background.

The detector is also capable, to a certain extent, of detecting photons via pair production, although this function is of secondary importance compared to Compton detection, see section 5.4 for more details.

4.3.1 Tracker properties

The tracker is made of multiple layers (20 initially, 30 in later designs) of DSSD, thus allowing the tracking of the electron and the reconstruction of the position of interaction on the xy plane, assuming they are stacked along the z-axis. Each layer is 500 µm thick, thus only a limited fraction of events (which depends on photon energy and incidence angle) have an electron energetic enough to leave a track. The pitch strip is initially set to 300 µm, which should allow good electron-tracking capabilities.
The tracker values where chosen similar to the ones for the *Fermi* LAT, since it performed well, and thus used as a starting point for the optimization process. We will briefly see how the tracker was improved in chapter 5, however, for a more detailed discussion on its optimization, see [10].

4.3.2 Calorimeter properties

Looking at Table 4.1, we can see that the CsI(Tl) is a material well suited for the calorimeter of a compact detector:

- Its high density, Moliéŕe radius[2] and radiation length allow a good energy absorption of the photons, even at higher energies.
- The scintillation decay time is relatively fast, although more decay components exist. The fastest has a decay time of 0.6 µs, while the slowest has a decay time of 3.5 µs. This allows an overall fast response of the calorimeter to photons.
- The wavelength of maximum emission is very convenient, since at that value CsI(Tl) crystals can be easily coupled to a photodiode readout.
- The CsI(Tl) scintillators are a cheap, yet reliable technology which is already well understood from its previous uses on detector such as the Fermi LAT.

Of course, CsI(Tl) is not the only choice for the calorimeter of a compact detector. For example, CZT has also been considered, but in the end, for the reasons above, CsI(Tl) was selected.

[2]The Moliére radius is a value characteristic of each material which quantifies what is the necessary radius of a cylinder of such material to contain (on average) the 90% of the energy of an electromagnetic shower initiated by a photon.

Density (g/cm^3)	4.51
Molieŕe radius (cm)	3.57
Radiation length (cm)	1.86
Wavelength of max emission (nm)	550
Lower wavelength cutoff (nm)	320
Primary decay time (ns)	1000
Light yield (ph/keV)	54

Table 4.1: CsI(Tl) crystal specifications.

4.3.3 Calorimeter read-out

The CsI(Tl) properties make it very convenient to be coupled to a photodiode, since the crystals have an emission peak at 550 nm, together with the fact that the photon yield is quite high.
For example, let us suppose to use $0.5\times0.5\times5\,\mathrm{cm}^3$ crystals. A crystal will be able to completely absorb photons up to a few MeV, depending on the angle of incidence.
To give a rough idea of the estimates involved, let us consider the crystal coupled to a common photodiode read-out (e.g. Hamamatsu S3590). For each keV of absorbed energy ∼360 e^- would be emitted in the photodiode, and a reading accuracy of ∼ 2.3 keV would be achieved. In Table 4.2, some rough estimates for the read-out performance are given.

Energy (keV)	Scintillation photons	e^- photodiode
100	$5.4\cdot10^3$	$3.6\cdot10^4$
500	$2.7\cdot10^4$	$1.8\cdot10^5$
1000	$5.4\cdot10^4$	$3.6\cdot10^5$
2000	$1.1\cdot10^5$	$7.2\cdot10^5$
3000	$1.6\cdot10^5$	$1.1\cdot10^6$
5000	$2.7\cdot10^5$	$1.8\cdot10^6$

Table 4.2: CsI(Tl) scintillation photons produced at various energies.

5 Detector and calorimeter optimization

5.1 First simulations

Starting from the basic design established in chapter 4, various different configurations have been tested. In particular, for each setup the detector has been tested with a mono-energetic point source at normal incidence (i.e. zenith angle $\theta = 0$), with energy set at 100, 333, 500, 1000, 2000 keV, in order to estimate the behavior of the detector as a function of the energy.
For a general idea of the performance of the detector at the early stages of optimization, particular attention has been given to the energy resolution and the ARM value, while a further analysis of the other variables, such as SPD, percentage of tracked events etc. has been delayed until there was a more finalized detector design.
The very first configuration simulated, had a tracker made of 20 5.9×5.9 cm^2 planes stacked along the z-axis, with thickness 500 µm and pitch of 300 µm for the strips. Technical limitations impose a minimum distance between silicon planes, since we need both a frame to keep them fixed and the space to insert the read-outs.
The calorimeter, instead, was made of two grids of 12×12 CsI(Tl) crystals on the xy plane, stacked along the z-axis. Each crystal is $0.5 \times 0.5 \times 1.8$ cm^3 big. The basic idea behind this setup, was that by having a relatively small tracker, the electron tracking capability could be retained while not sacrificing too much space and budget to the tracker module. For the calorimeter, instead, multiple planes of relatively thin crystals should (in principle) provide a better position measurement for the scattered photon, but this did come at expense of the energy absorption of the photon, which ended up worsening the overall detector performance, as we will see from the results of the first simulations.

The calorimeter's crystals depth resolution (i.e. the resolution of their position of interaction measurement) is set to 1.5 cm for the first design, close to the value for the *Fermi* LAT. In subsection 5.2.5 we will see how much this parameter changes the overall performance of the detector. For the first setups, the trigger used was a very simple one, requiring only a hit in both tracker and calorimeter. In Figure 5.1, we can see the detector design.

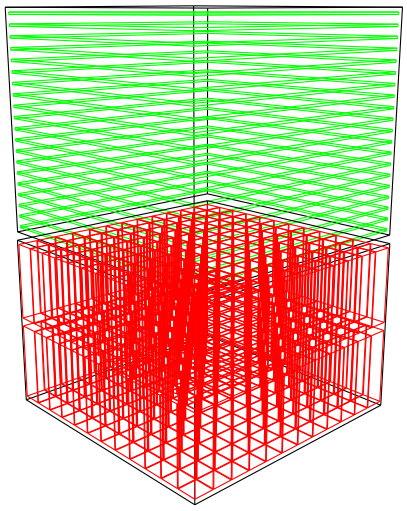

Figure 5.1: Initial detector design.

For the sake of brevity not all of the simulated sources will be presented; to illustrate the rough behavior of the detector and its main issues, we will take a look at the spectra of 100, 1000 and 2000 keV, so as to have a basic understanding of the performance dependence on energy. For a very rough, but quick, evaluation of the detector, we can limit ourselves to checking the energy and ARM spectra, since several important issues can already be pointed out from just those.
In Figure 5.2 we can see the spectra resulting from the simulations. Even without looking in great detail at the simulation results, we can see that the detector performance is rather poor with this design. The capability of the calorimeter of absorbing the scattered photon is scarce, especially with higher energy (2000 keV) photons, furthermore the ARM peak is very wide, especially at 100 keV, where it is basically unusable.

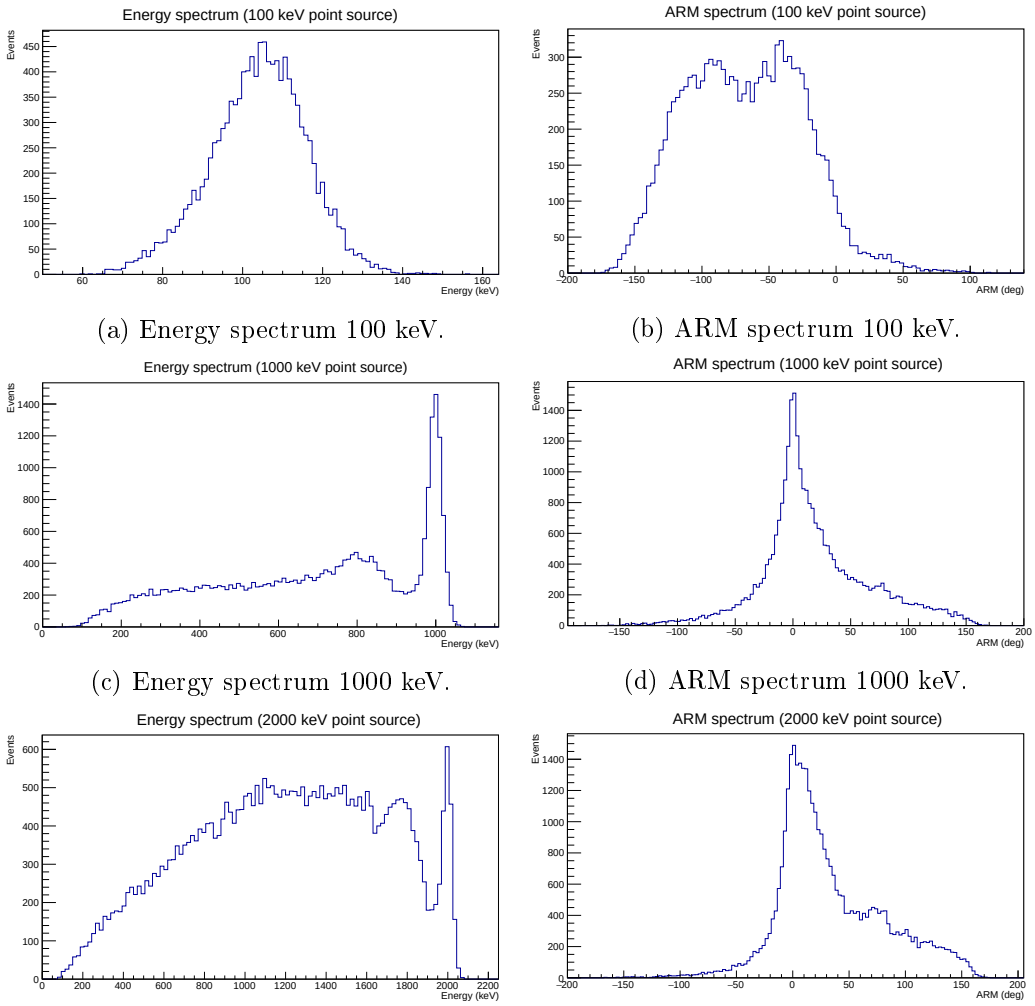

(a) Energy spectrum 100 keV.

(b) ARM spectrum 100 keV.

(c) Energy spectrum 1000 keV.

(d) ARM spectrum 1000 keV.

(e) Energy spectrum 2000 keV.

(f) ARM spectrum 2000 keV.

Figure 5.2: Example spectra from the first detector design batch of simulations.

To improve the performance, the first thing to do is to increase the size of the calorimeter's crystals to improve the energy absorption capability. As for the tracker, we can increase the number of layers and decrease the pitch of the strips to obtain both better tracking capability and more probability of interaction (since the tracker is overall thicker). Specifically, the layers were increased to 30 and the pitch decreased to 150 µm (for further details on the tracker optimization see [10]). Additionally, to make full use of the volume at our disposal and improve the effective area, the tracker layers were increased in area to $8.2 \times 8.2\,\mathrm{cm}^2$.

Note however that we cannot occupy the full volume of the CubeSats, since both on-board electronics and a frame to keep the various parts fixed are needed.
For the calorimeter, various configurations have been tested, making the crystals thicker and/or longer and using only one instead of two layers. The best result, however, were achieved with a single grid of $1\times1\times5\,\mathrm{cm}^3$ CsI(Tl) crystals. This of course means that we have less crystals, which could, in principle, worsen the ARM. However, the benefit of having a better energy absorption surpasses by far the con, as we will see in section 5.2.

In the next section we will see how these changes impact the overall performance of the detector.

5.2 Improving the detector basic design

Using the improvements listed in the previous section, the detector was redesigned, as we can see in Figure 5.3.

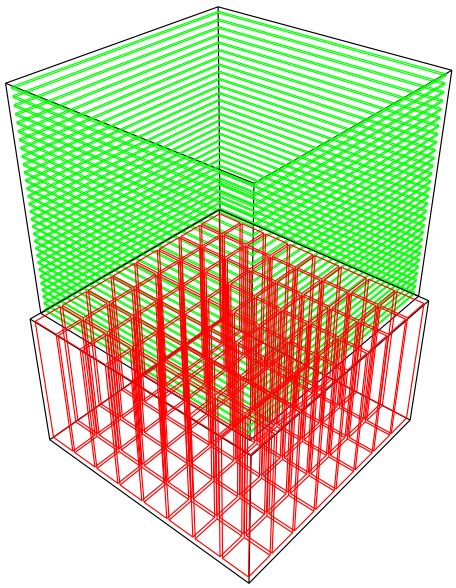

Figure 5.3: Improved detector design.

A very important limitation of the previous detector's design was the number of incompletely absorbed photons, the "tail" of the energy spectra. Although the small volume we can use limits the size of the calorimeter, it is important to make sure that there is a good compromise in the crystals' size and their number.
While having more crystals could improve the ARM, having a good energy absorption capability is even more important, since otherwise the Compton sequence will be wrongly reconstructed; thus the crystals cannot be made too thin.

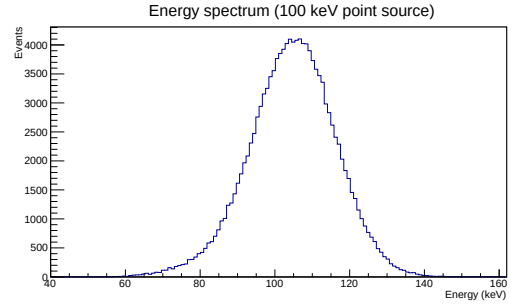

(a) Energy spectrum 100 keV.

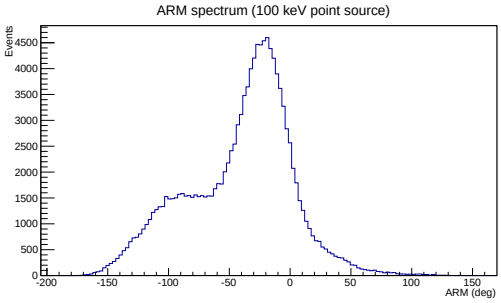

(b) ARM spectrum 100 keV.

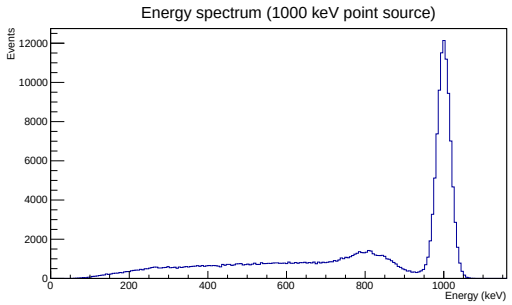

(c) Energy spectrum 1000 keV.

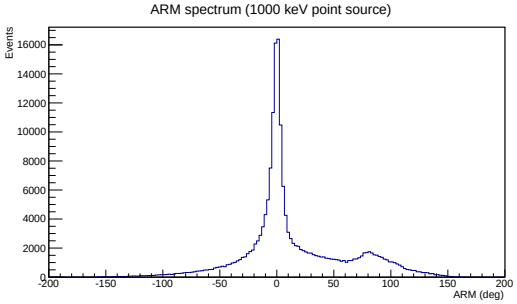

(d) ARM spectrum 1000 keV.

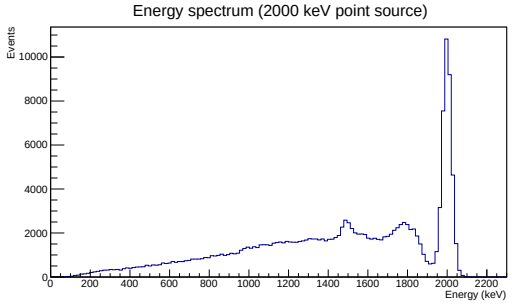

(e) Energy spectrum 2000 keV.

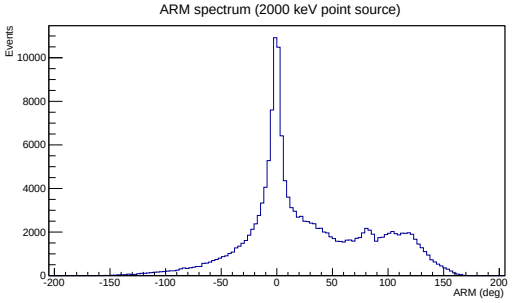

(f) ARM spectrum 2000 keV.

Figure 5.4: Example spectra from the simulations for the improved detector design.

Just a quick glance at Figure 5.4 is enough to understand how much the performance has changed with this design. The energy absorption has been greatly improved, with far less incompletely absorbed events, while the ARM distribution's shape has now smaller tails and a narrower peak.

Additionally, we are now able to provide a rough estimate of the energy resolution and angular resolution. While to compute the energy resolution, we can simply use a gaussian fit of the core peak[1], the case of the ARM is a bit more complicated, since the shape of the peak is not similar to that of any simple distribution, however a good estimate of the peak FWHM can be provided by a fit with two distinct gauss distributions for each side of the ARM core peak.

In Table 5.1 we can see some preliminary values (hence the omitted uncertainties, which do not affect the comparison between different designs), without any quality cut applied. The ARM bias is the distance of the maximum of the peak from the 0 of the distribution (which represents a perfectly correct direction measurement for the photon).

Energy (keV)	E_{res} (%)	ARM_{FWHM} (°)	ARM_{bias} (°)
100	24.8	51.5	-24.2
333	9.3	12.9	-0.8
500	6.8	9.9	-0.3
1000	4.2	8.6	-0.3
2000	2.7	11.5	-0.7

Table 5.1: Fit results for energy and ARM spectra.

These values, meant only to give some rough basis of comparison for later designs, already tell us that the detector performance are very sensitive to the energy, and at 100 keV we already reach the limits of the current design. The performance seem instead to peak around 1 MeV, which further supports the idea that the basic design is indeed correct for our purpose.

[1] A fit of only the full absorption peak is motivated by the fact that the partial absorbed events are a part of the data we wish to exclude (or at least greatly reduce) using cuts on later stages of the work, which is outside the scope of this thesis. The same reasoning is also applied to the fit of the ARM peak. In a finalized design, after applying the quality cuts, we would however need to also estimate the tails, for example by using containment intervals.

5.2.1 Computing the effective area

Although the design is still far from being finalized, it is nonetheless still interesting to compute the effective area for the detector at each energy, so to have some preliminary values to compare with later designs and see which performs better. Note that this is a bit of a delicate matter, since it is not enough to just increase the effective area (i.e. increase the data acquired) to state that a design is better than another, the quality of the events must also be kept in check, since if the additional data acquired ends up being composed mostly of poorly reconstructed events, the detector would end up performing worse or, at best, after the quality cuts, as well as before. This is of course an aspect which was taken in account during the optimization process.

Since the sources simulated so far are particularly simple, the effective area can easily be calculated by the following equation:

$$A_{eff} = \frac{N_{obs}}{\Delta t \cdot F} \tag{5.1}$$

where N_{obs} is the number of observed events, Δt is the total observation time for the source and F is the simulated flux of the source. Notice that, for now, N_{obs} includes all measured events, without quality cuts, which will instead be taken into account for the later designs of the detector, see section 5.3 for example.

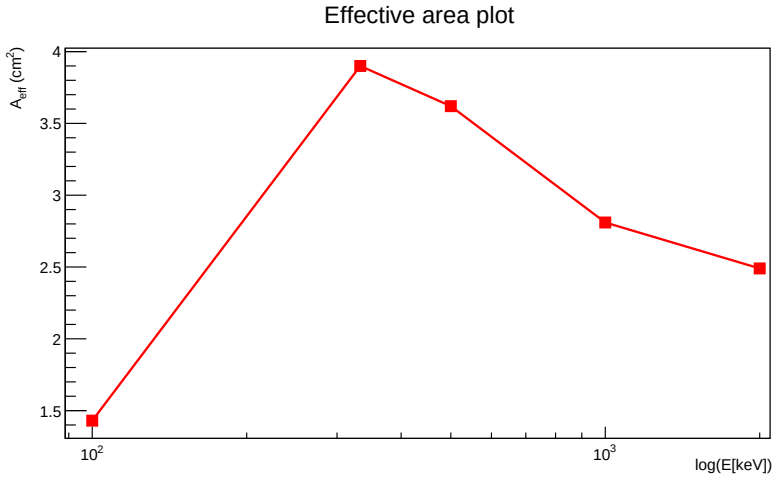

Figure 5.5: Plot of the dependence of effective area from energy.

In Figure 5.5 we can see the effective area values for the simulated spectrum. The errors, given only by the statistics of the simulations[2], are very small ($\sim 10^{-3}$ cm^3) and not plotted. The effective area increases rapidly from 100 keV to 333-500 keV and then starts to slowly decrease. This is mostly due to the fact that, both at lower and higher energies, the Compton cross section is getting smaller, thus less events are triggered.
These preliminary values should not be taken as representative of the final performance, but they are nonetheless a good way to estimate a design performance when making a comparison between alternative setups (as we will see in subsection 5.2.3), since a design having more effective area is, of course, preferable to one having less, as long as the data quality remains unchanged. It must be remembered, however, that the effective area is only one of the final parameters of the space telescope, together with angular resolution, sensitivity, percentage of tracked events etc, which must be all taken in account in the end.

5.2.2 The calorimeter-only detector

Given the results of the first batch of simulations, it is of interest to understand how much the presence of a tracker changes the overall performance of the detector. In fact, a detector made only of a calorimeter was tested. The following is, of course, not a realistic detector design, but it is still a useful check to see how much the tracker improves the detector's overall performance, and how much a bigger calorimeter improves the photon absorption.

With this design, the calorimeter occupies all the volume, with a grid of 18×18 CsI(Tl) crystals, each 0.5×0.5×10 cm^3 big. As we would expect, this configuration has better energy absorption, but at the expense of the complete loss of the electron tracking capability.

In Figure 5.6, we can see how the detector behaves at different energies. At low energy ($E = 100$ keV) the calorimeter does not perform very well even in the energy measurements, while the ARM spectrum is completely unusable. The situation improves at intermediate energies, where we can see that both the ARM and the energy absorption peak become narrower. The ARM plot is, however, still far inferior compared to the ones from the tracking-detector simulations.

[2]In a completely finalized design, all the characteristics of the detector would be specified and it would also be possible to compute the systematic uncertainties. Here, however, we are only discussing prototypes for which the read-outs and the electronics have yet to be decided, thus the only uncertainties considered are the statistical ones.

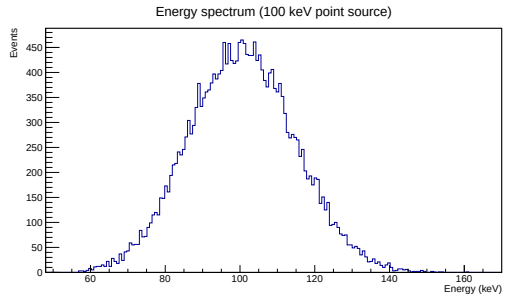

(a) Energy spectrum 100 keV.

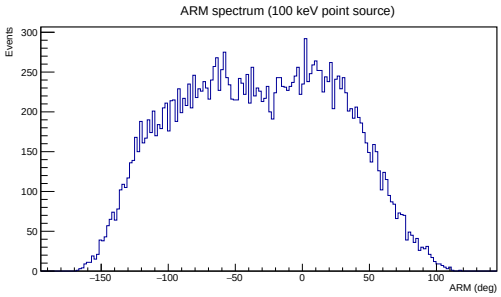

(b) ARM spectrum 100 keV.

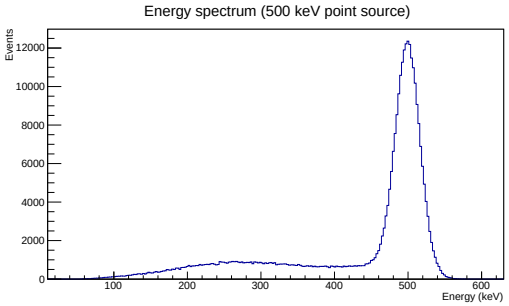

(c) Energy spectrum 500 keV.

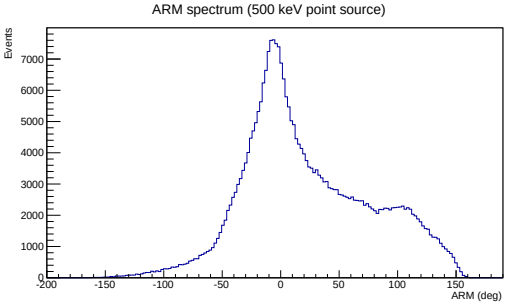

(d) ARM spectrum 500 keV.

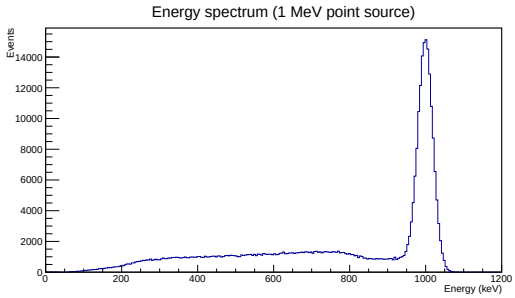

(e) Energy spectrum 1 MeV.

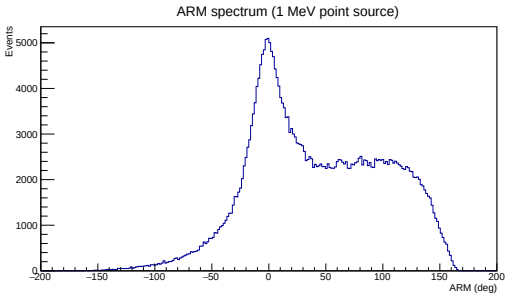

(f) ARM spectrum 1 MeV.

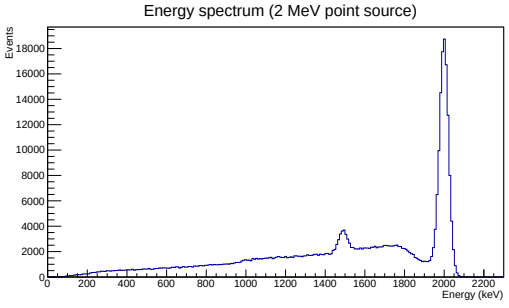

(g) Energy spectrum 2 MeV.

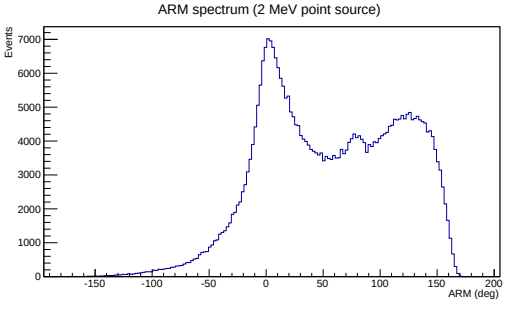

(h) ARM spectrum 2 MeV.

Figure 5.6: Examples of energy and ARM spectra for the only-calorimeter detector (all at normal incidence).

Finally, at higher energies (1-2 MeV), the detector performance starts worsening once again, with a lot of incompletely absorbed photons and electrons. The little peak at ∼1.5 MeV, visible only in the 2 MeV energy spectrum, is a *single escape peak*. This happens when a photon (of $E \geq 2m_e c^2 = 1.022$ MeV) creates a pair e^+e^- and, when the positron annihilates, one of the emitted photons escapes from the detector, so the event is misclassified as a Compton. It is also possible (although less likely) that both photons escape the detector. The corresponding peak, which is too small to be visible in this simulated spectrum, is called *double escape peak*.
What we can deduce from the energy spectra is that the energy absorption with a calorimeter-only detector, although surely better, is not that much different from the one of the improved design of section 5.2. Furthermore, if we compute the energy resolution, we see that it remains nearly unchanged.

Finally, as visible in Figure 5.7, the effective area of the calorimeter-only design is much bigger then the previous design, but this is not taking in account in any way the poor quality of the data thus obtained.

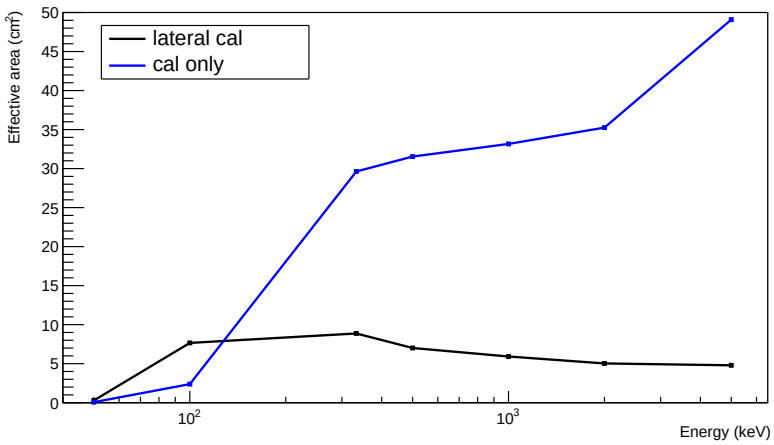

Figure 5.7: Plot of calorimeter-only detector and tracking-detector effective area.

What we can deduce from the plots is that the presence of a tracker unit in the detector is well motivated, since without it there is no electron tracking capability at all, and we surely could not reach COMPTEL's level of performance using a CubeSat.

5.2.3 The lateral calorimeter

An issue with the detector designs seen so far is that a lot of possible good events are lost at the edge of the tracker. This is easily seen by looking at Figure 5.8, where a projection on the xy plane of the tracker events can be seen.

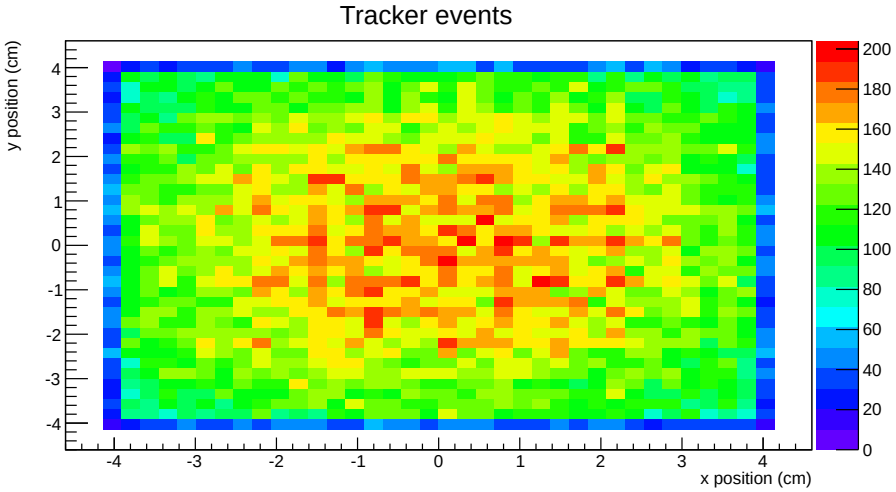

Figure 5.8: Plot of the xy event distribution on the tracker (point source with normal incidence).

It is easy to see that this design is not taking fully advantage of the tracker size, since a significant fraction of events are lost at the edge. If the incoming photon interacts near the edge of the tracker, there is a high chance that the scattered photon will exit the tracker. This issue can be solved if a lateral calorimeter is added, thus allowing to trigger events which would otherwise have left the detector.

Along these lines, two different designs have been tested, one where the tracker was shortened of 0.8 cm on both the x and y side, and one with a reduction of 1.8 cm. In Figure 5.9 we can see one of such designs, where the lateral calorimeter crystals are 1×1 cm^2 wide and high enough to cover all the side of the tracker, plus $\sim$1 cm of overlap with the bottom calorimeter.

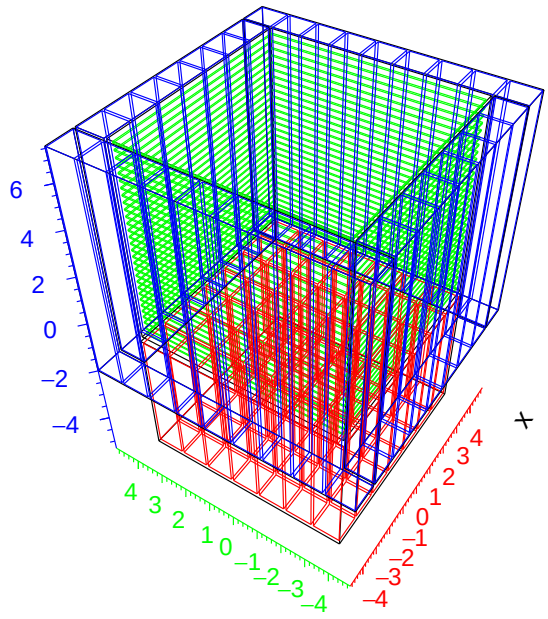

Figure 5.9: Detector model with lateral calorimeter.

A quick comparison of the performance for the designs can be made through their effective area, since no other property of the detector is significantly affected by this change.
We can see the results in Figure 5.10, where it is evident that the setups with lateral calorimeter perform much better. In particular, the one with the smaller tracker reduction is the one with greatest effective area.
After choosing to continue with that design, the trigger was updated to also include events with a hit both in the lateral calorimeter and the bottom calorimeter, instead of always requiring a hit in the tracker.

Note that this also changes the effective area values, since, keeping all the other conditions the same, we now accept more events. Although the calorimeter-calorimeter events are observed to have an overall worse ARM, it was still decided to keep them, since such a trigger is particularly helpful when acquiring data at higher energies (smaller Silicon Compton cross section).

Moreover, if needed, events triggered in such a way can be discarded during the data analysis.

One final thing that needs to be pointed out is that the overall performance of the detector worsens dramatically below 100 keV, as we can see, for example, from the effective area in plot. The energy resolution and angular resolution are also greatly affected.
This is a consequence of the choice of materials for the detector, whose performance greatly decreases at lower energy (especially true for the CsI(Tl) calorimeter). This is, however, not a major problem, since we need the best performance around 1 MeV. For a more complete study of the final performance of this design as a function of the energy and the zenith angle, see chapter 6.

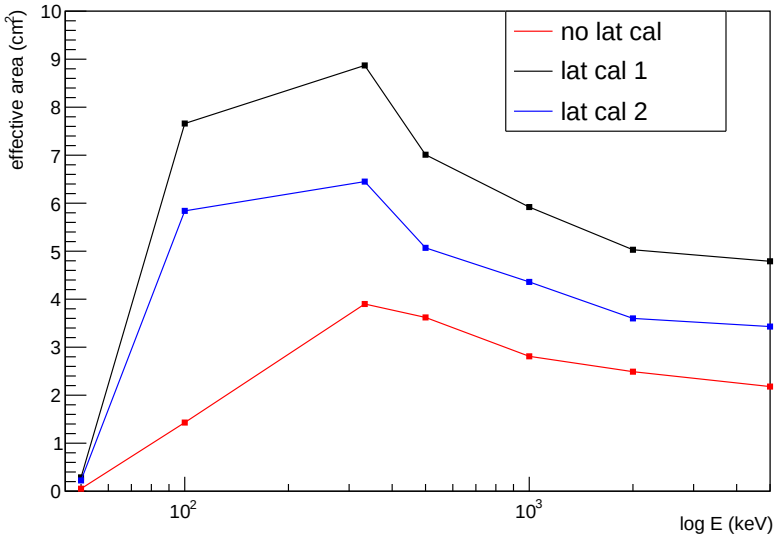

Figure 5.10: Comparison between the two detector with lateral calorimeter and the one without (lat cal 1 is the one with more tracker surface).

5.2.4 Tracked events

Before proceeding in the discussion of the calorimeter optimization, we will briefly introduce the tracked events, which will be studied more extensively in section 6.2. Tracked events are the most important part of our data, since they can provide much better information on the source compared to COMPTEL-type events, which do not possess a track. The downside is, of course, that they only represent a small fraction of the total data, how much depends on both the energy and the zenith angle (we will see the numbers in detail in chapter 6). At 1 MeV, for example, we have ∼20% of tracked events, which energy and ARM spectra we can see in Figure 5.11.

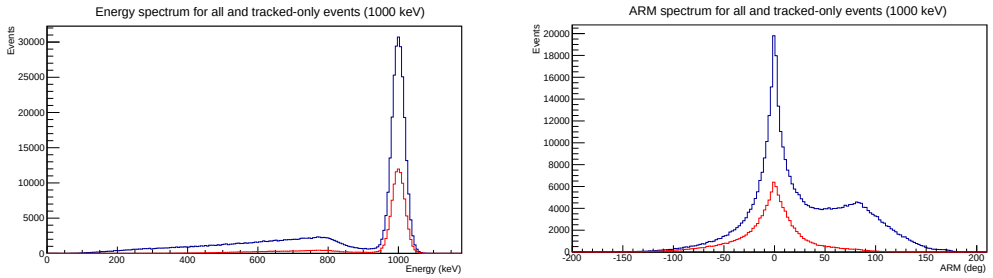

(a) Energy spectrum 1000 keV

(b) ARM spectrum 1000 keV

Figure 5.11: Energy and ARM spectra for all (blue) and tracked events (red).

As we can see, although a lot of events are lost, the ones left have a more complete energy absorption and a more symmetrical ARM distribution (although the FWHM of the peak is slightly bigger for the tracked events). In Figure 5.12 we can also see the corresponding SPD spectrum.

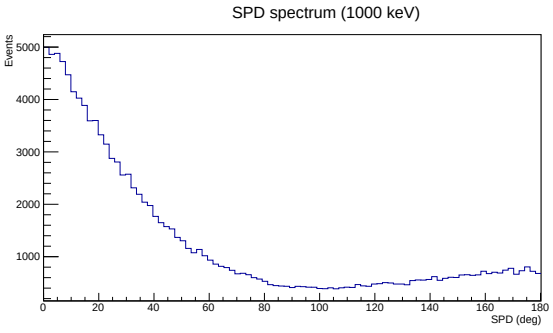

Figure 5.12: SPD distribution for a 1000 keV point source at normal incidence.

Note the using the SPD we have a gain in angular resolution, since for the untracked events the SPD is 180° wide.

5.2.5 Depth resolution of the calorimeter

Another important parameter to consider for the calorimeter optimization is its depth resolution, and how it does impact the detector performance.
To evaluate this, three different configurations have been tested, with depth resolution 1.5, 1.0 and 0.5 cm. For reference, the *Fermi* LAT achieved a depth resolution of 1.5 cm in its calorimeter's crystals, but there is most likely room for improvement.

Regarding the simulations, for each setup a fit of the ARM, SPD and full energy absorption peak was done, in order to evaluate the different performance. More precisely, a point source of 1000 keV at normal incidence was simulated, and of the measured events only the tracked ones have been considered. Of particular interest were the ARM and SPD spectra, which were fitted through Mimrec, from the MEGAlib library.

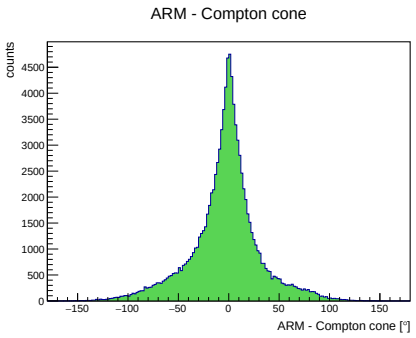

(a) ARM for depth resolution 1.5 cm

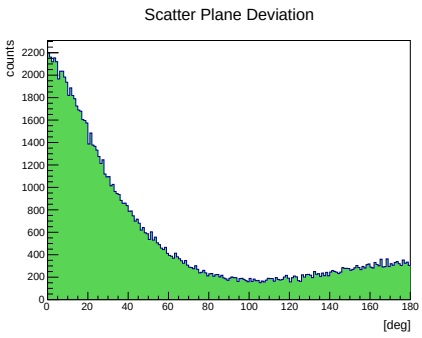

(b) SPD for depth resolution 1.5 cm

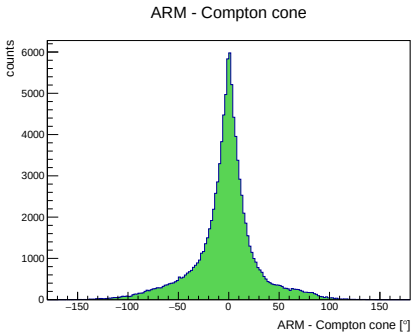

(c) ARM for depth resolution 1.0 cm

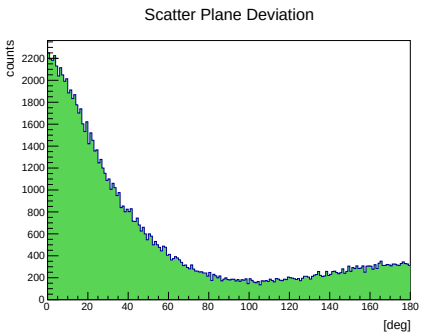

(d) SPD for depth resolution 1.0 cm

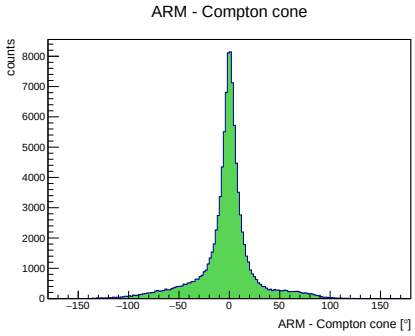

(e) ARM for depth resolution 0.5 cm

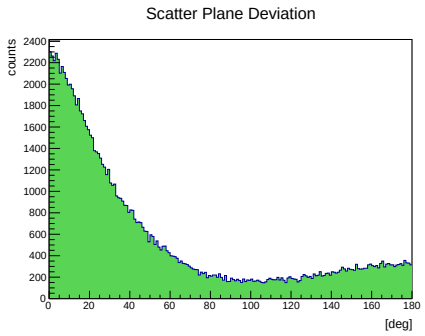

(f) SPD for depth resolution 0.5 cm

Figure 5.13: ARM and SPD spectra at different depth resolutions.

As visible Figure 5.13, with a better depth resolution the shape of the ARM spectrum improves noticeably, with the peak getting narrower, while the SPD remains roughly the same. This is reflected in the values obtained from the fits, which are listed in Table 5.2. In the table, we can see the ARM FWHM bias (i.e. the position of the fitted function maximum with respect to the 0 of the spectrum) and the 68% containment interval value, which is the half-length of the interval, with center in 0°. Since the results are only meant to give the rough behavior of the detector in function of the depth resolution, no uncertainties (which do not affect the comparison) are given.

Depth res (cm)	ARM FWHM (°)	Bias (°)	ARM 68% (°)
1.5	27.5	0.38	27
1.0	20.3	0.17	23
0.5	15.4	0.15	17

Table 5.2: Fit results for ARM spectra.

In Table 5.3 the fit results for SPD and energy spectra are visible, where there are small to no changes in their behavior at different depth resolution.

Depth res (cm)	SPD FWHM (°)	SPD 68% (°)	$\frac{\Delta E}{E}$(%)
1.5	60.0	53.5	4.4
1.0	60.8	52.5	4.4
0.5	59.6	51.5	4.4

Table 5.3: Fit results for SPD and energy resolution.

It is evident that the depth resolution of the calorimeter's crystals has a big impact on the ARM, which means a better localization of the source and also less background, since, if the detector can measure the source position with greater accuracy, less background events are included while trying to reconstruct the source's flux.
Improving the depth resolution for the calorimeter may thus increase the overall detector performance significantly, especially the sensitivity.

5.3 Quality cuts

So far, no quality cuts have been considered for the simulated spectra, since the designs were very preliminary and only meant to give a rough idea of the detector performance. However, for a realistic detector, quality cuts are needed to remove poorly reconstructed events.
Although background contributions will only be introduced in chapter 6, we can still apply some preliminary cuts to remove poorly reconstructed events, which are present with or without the background.
The design considered here is the one including the lateral calorimeter, with a depth resolution of 1.5 cm for the crystals. The quality cut procedure was approached in two different ways: first with a manual check of the data, after that, to further improve the cuts, an automated method was applied.

5.3.1 Manual quality cuts

For this part of the work, the reconstructed events have been checked manually, looking for some kind of easily recognizable signature for bad events. For example, it was noticed that events with a sequence length (i.e. number of interactions in the detector) greater than 5 appeared to be mostly poorly reconstructed, and where thus discarded. In other cases, instead, more complicated combinations of the basic kinematic variables have been tested, but their effectiveness was often dependent on the particular energy considered.

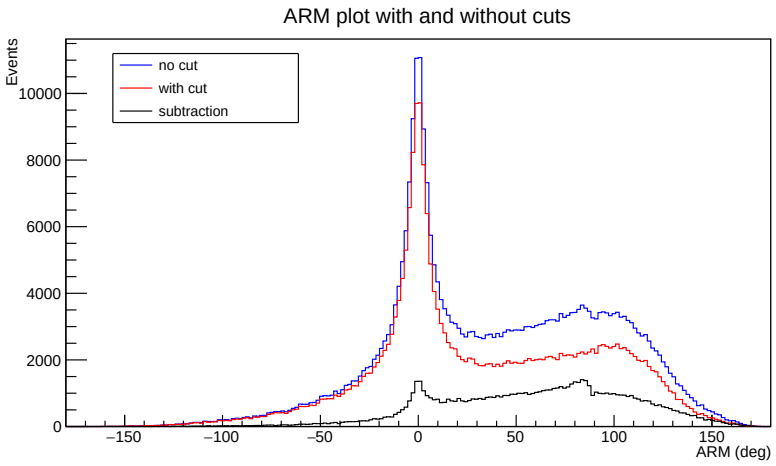

Figure 5.14: 2000 keV ARM spectrum with and without cuts.

The results were particularly good for the ARM spectrum at higher energies, for example at 2000 keV, as we can see in Figure 5.14. However, if we check instead the energy spectrum, using the same cuts, we can see that the results were not as good. As visible in Figure 5.15, many good events (the ones with full energy absorption) are discarded in the process, and the cuts seem to apply more or less to the same degree to all of the energy spectrum.

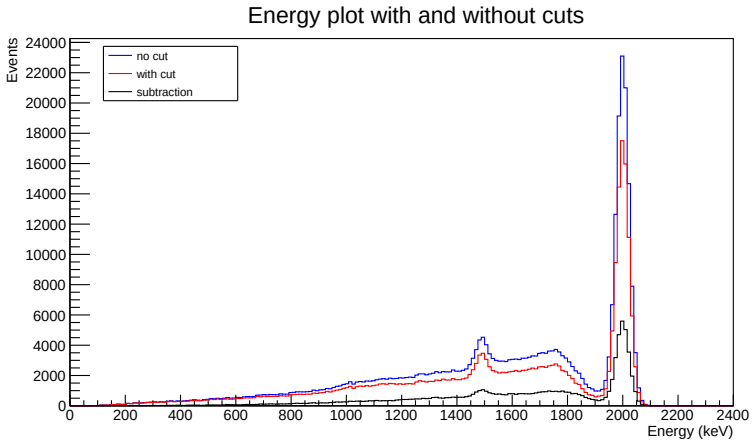

Figure 5.15: 2000 keV ARM spectrum with and without cuts.

In Figure 5.16 we can instead see the effective area after the cuts.

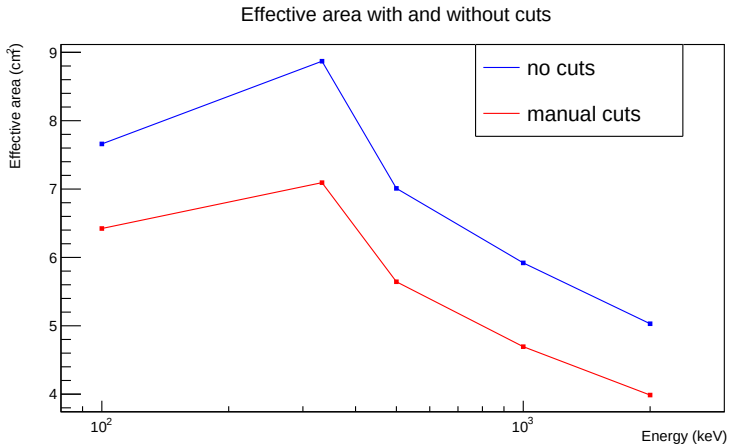

Figure 5.16: Effective area with and without cuts.

The cuts were done by discarding a maximum of ∼20% of the total events, less if there were not so many wrongly reconstructed events. Overall, although the cuts do decrease the effective area, they are still worth using to improve the quality of the data.

5.3.2 Automated quality cuts

Since for each simulation there is a huge number of variables combinations to be considered, it's impossible to check every meaningful possibility manually. To overcome this problem, an automated approach to quality cuts has been used through TMVA (*Tool for MultiVariate Analysis* for ROOT). In particular, the *boosted decision tree* (BDT) method was chosen, which is a type of machine learning where a training data sample (i.e. a fraction of the actual real data) is manually divided in a signal part and in a background part. This data is the input from which the BDT starts. From that point, the BDT tests a variety of variables and checks how much statistical significance they hold when trying to separate signal and background.

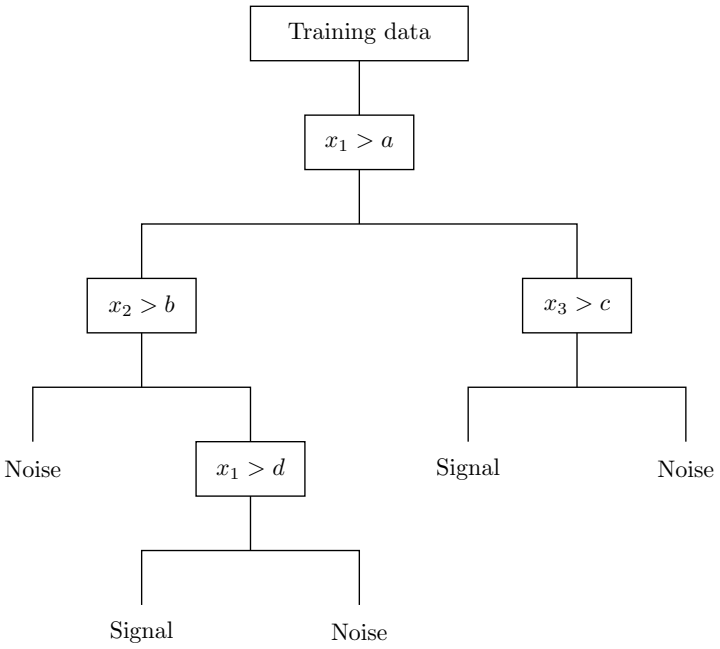

Figure 5.17: Boosted decision tree.

For this preliminary analysis we kept the complexity of the BDT small, so a single tree with few branches was created, so that we could recover the cuts and inspect them to obtain useful informations on the most effective variables. The single cuts are actually very simple: the BDT simply divides the data in two sets, one which has the variable x greater than a certain threshold, the other has x lower than that same value. Each time the data set is split into two parts, and the procedure is repeated n times, where n is the number of tree nodes, which can be decided by the user. The final structure for the data is that of a tree (as in Figure 5.17), in which each node splits the data in two parts. Each branch of such tree always ends by identifying the data as either signal or background. With this method, a list of variables, ordered by statistical importance (i.e. how much they are used to separate signal to background), is computed, based on how many times a node containing that variable appeared and how effective it was in separating signal and background.
This method, applied to training data sample, allows the machine to formulate a signal-background separation method on its own, which can then be applied to the rest of the data. How many variables are to be considered is decided by the user.

This approach has the obvious advantage of being able to test far more cuts combinations than by manually searching them, but of course (at least initially) the results need to be manually checked to see if everything is working correctly.
This method has been applied to see if the quality of the data could further be improved from the manual cut results. In particular, the data has been divided in events with |ARM| $\leq$20 (signal) and |ARM| $>$20 (background). This splitting, although somewhat simplistic, is still a good way to test if the method works.
To further improve the effectiveness of this approach, various other composite variables were added, other than the simple kinematic ones: for example, using not only E_g and E_e, but also E_e/E_g, $E_e \cdot E_g$ and $E_e - E_g$. Of all such composite variables, only some will be meaningful for the signal-background distinction, however using an automated method allows us to check them all and see which ones achieve the desired results.

In Figure 5.18 we can see the result of the BDT applied on the simulation data of a 2000 keV source, still discarding a maximum of $\sim$20% of the total data. Compared to Figure 5.14, we can see that there has been a great improvement, with more bad events discarded while sacrificing less good data (i.e. the events in the ARM peak).

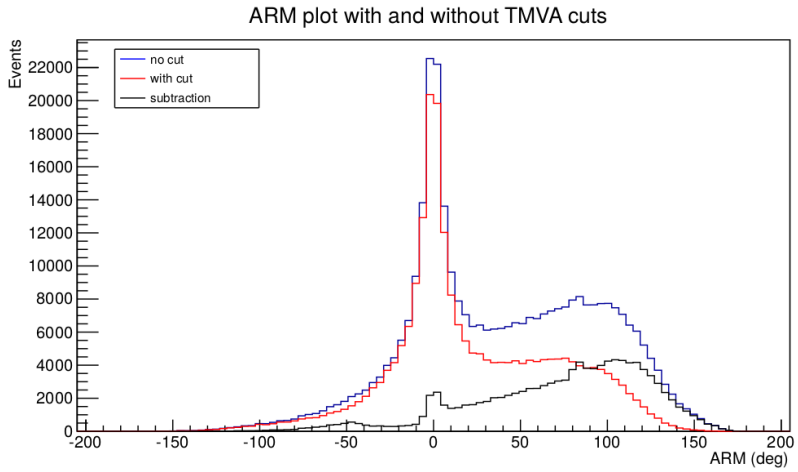

Figure 5.18: ARM TMVA cuts at 2000 keV.

Regarding instead the energy spectrum, we can see that the results obtained from TMVA cuts are rather similar to the ones obtained from the manual cuts, as we can in Figure 5.19.

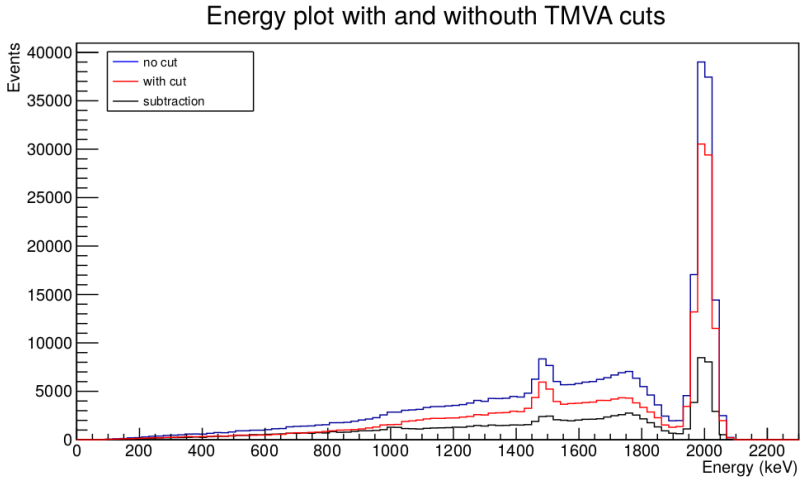

Figure 5.19: Energy TMVA cuts at 2000 keV.

At lower energies, the TMVA cuts are still effective, although to a lesser degree. However, sometimes they end up achieving worse results than the manual cuts, thus using a BDT is certainly a method with a lot of potential, but is a very delicate procedure.

5.4 Pair detection

As already hinted before, the detector is also capable to detect photons (of $E \geq 1.022$ MeV) through pair production, however, since its priority is to detect photons in the Compton region (i.e. via Compton scattering), the performance of the detector for pairs is inferior. This is mainly because the pair production cross section offered by the tracker planes is very small, thus at high energy a lot of photons just get through the tracker unit without interacting. Since tracking the e^-e^+ is fundamental for a pair-production telescope, this means that a lot of events are lost, thus we have a much smaller effective area.

In a dedicated pair-production telescope, such as the Fermi LAT, this problem is solved by adding layers of a high Z material, Tungsten in the LAT case.
This greatly increases the cross section, but the downside is that e^-e^+ generated by lower energy photons tend to be scattered by such layers, thus worsening the resolution of the detector at such energies. This issue, while tolerable for high energy pairs, would completely ruin the detector's capability of reconstructing the low energy Compton events.
Hence, such strategy could not be adopted for the detector.

Pair production simulations were made for 2, 3, 4, 5, 8 and 10 MeV point sources with normal incidence. In Figure 5.20 are shown the energy spectra and differential PSF[3] for pairs at 2, 4 and 8 MeV.

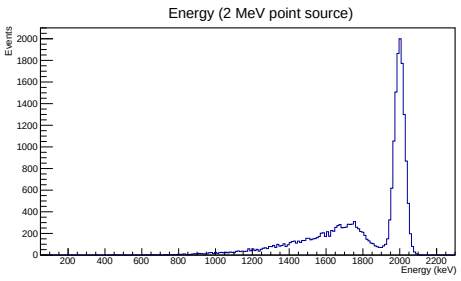

(a) Pairs energy spectrum 2 MeV

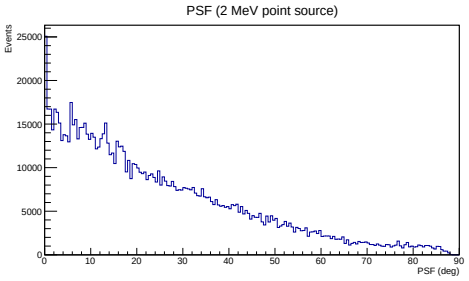

(b) Pairs PSF spectrum 2 MeV

[3]The *Point Spread Function* (PSF) describes how well the detector can reconstruct the initial photon direction. The ones in the plots are differential PSFs, meaning that each bin was normalized with the respective solid angle interval.

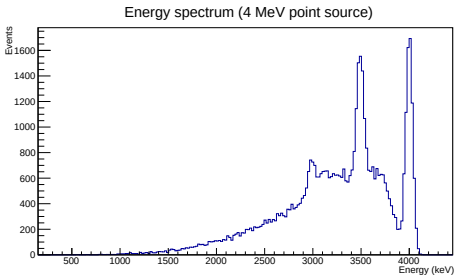

(c) Pairs energy spectrum 4 MeV

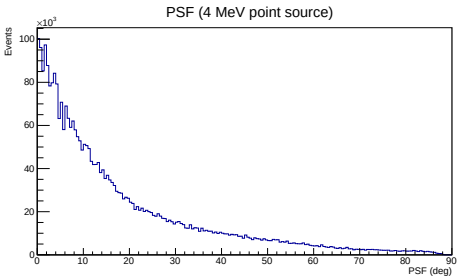

(d) Pairs PSF spectrum 4 MeV

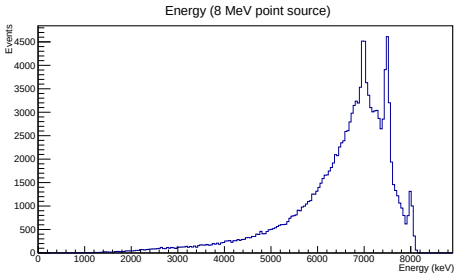

(e) Pairs energy spectrum 8 MeV

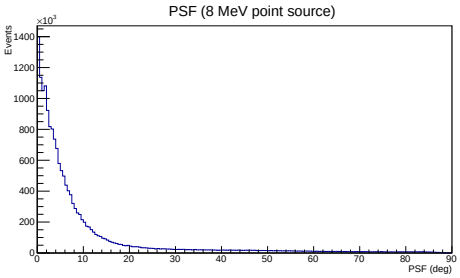

(f) Pairs PSF spectrum 8 MeV

Figure 5.20: ARM and SPD spectra at different depth resolutions.

As visible in the plots, the energy spectra become a lot worse at higher energies, with incomplete absorption becoming a more and more relevant issue.
The PSF's peak becomes instead narrower with increasing energy, since it is easier to track higher energy positrons and electrons.
Some preliminary cuts have also been tested, with the purpose of discarding poorly reconstructed events and improving the PSF, although the only cut applied in the end was for the electron and positron directions.
The effective area associated with the pair production can also be compared to the Compton effective area, the results of which can be seen in Figure 5.21. As we can see, the effective area for the pairs is much smaller than the one for Compton, although it increases with energy due to the pair production cross section getting bigger.
It must be noted, however, that these values still include a lot of events with incomplete energy absorption, which is particularly evident for the pair events at higher energies. Although we can still retrieve a direction measurement for the pairs at higher energies (i.e. several MeV), the energy absorption gets worse and worse. This is a fundamental limit of a compact detector design, since we would need more material to fully absorb higher energy photon. However, since we have precise weight and volume restrictions, it is not possible to improve much the energy absorption.

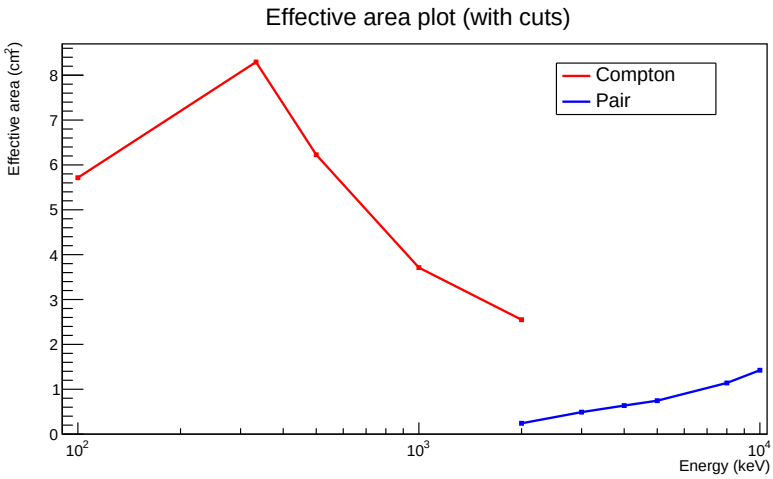

Figure 5.21: Total effective area of the telescope (with preliminary cuts).

In the end, pair detection is of secondary importance, since the primary scope of the detector is Compton detection and so it won't be discussed any further.

6 Events classification and background

In the previous chapter, we saw how the detector has been progressively improved starting from a very basic design. In the process, however, some important issues have been neglected, such as the detector's performance dependence on the zenith angle and the impact of the background to the data. In this chapter we will focus on these two main aspects: the different performance of the detector depending of the type of events selected and the simulation of the background.

6.1 Simulating all energies and angles

To improve the simulation method, and obtain more data on the space telescope's performance, the next step is to simulate sources at various zenith angles with respect to the detector.
Instead of simulating many point sources at different energies and inclinations, it is however faster to simulate a diffuse source uniformly covering the target phase space, which we will call *allgamma* in the plots. To this purpose, we simulated a diffuse source covering the entire upper half of the sky in detector coordinates, and the energy range from 100 keV to 10 MeV. We configured it to have uniform emission in solid angle (i.e. in $\cos\theta$), with a *power law* spectrum of energy index -1 (i.e. with constant emission per energy decade). Written explicitly:

$$\frac{dN}{dE} = N_0 \left(\frac{E}{E_0}\right)^{\gamma} \tag{6.1}$$

where N is the number of emitted photons, E is the energy, γ is the energy index, N_0 and E_0 are constants.
In this chapter we assume a satellite orbiting in zenith-pointing mode, i.e. with axis oriented to the zenith and back to the Earth.

A plot of the measured spectrum is visible in Figure 6.1.

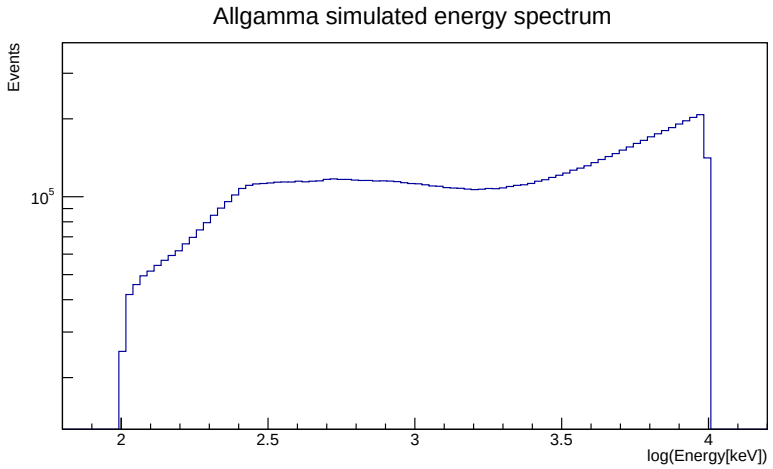

Figure 6.1: Measured energy spectrum in log scale.

In Figure 6.2 we can instead see a plot of the diffuse source energy vs. direction of the events (as measured by the detector, not as emitted by the source).
We can notice how there is a roughly uniform statistic in each bin, especially for the middle range of the energy spectrum (300 keV $\lesssim$ E $\lesssim$ 3 MeV), which covers the region of most interest for us.

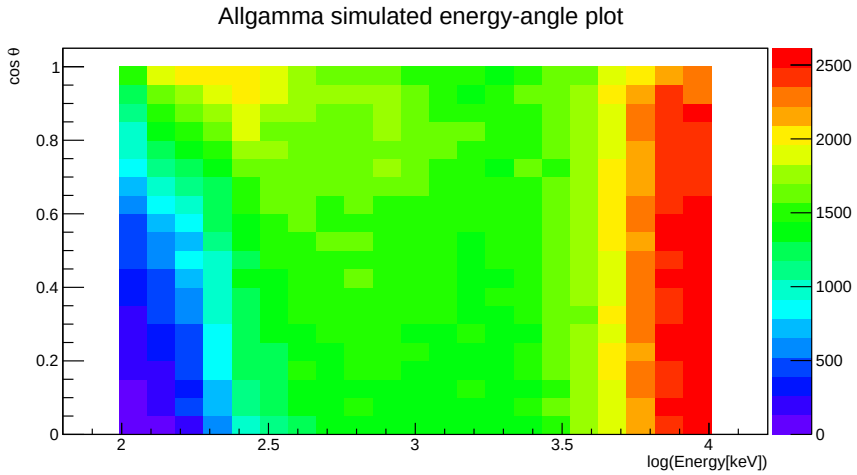

Figure 6.2: Measured energy-cos θ plot.

6.2 Event classes

In the previous plots we either kept all events or selected the tracked ones. It is however interesting to deepen a bit our understanding of the detector's performance in function of the classes of events chosen. Up to now only minor quality cuts were taken into account, removing the events that were clearly reconstructed badly, so it is important now to choose classes of events which behave in a sufficiently "good" way, meaning we require that all distributions (energy resolution, ARM, SPD) present a pronounced core we can fit, allowing for some tails we can hope to remove in the future. It would be pointless, for example, to try to fit the tiny full energy absorption peak for a source at 10 MeV before making some very heavy cuts. Thus, with exception of class 3, the main focus of this thesis will be on tracked events, which provide data of overall better quality than the others. Four classes of events were thus defined:

- **Class 0**: all of the tracked events.
- **Class 1**: tracked events which did not have an hit in the lateral calorimeter. Subset of class 0.
- **Class 2**: tracked events which did not have an hit in the bottom calorimeter. Subset of class 0.
- **Class 3**: events with at least one hit in both tracker and bottom calorimeter, but none in the lateral calorimeter, thus this is not a subset of class 0.

To proceed to the calculation of the performance parameters, we need to divide the diffuse simulation data in bins of energy and zenith angle. A good compromise between number of bins and their statistics was achieved by dividing both the $\log E$ and $\cos\theta$ in 8 intervals each. For each bin of of each class we can then fit the spectra to obtain energy resolution, ARM and SPD (when only tracked events are being considered).
Since only some minor quality cuts have been applied to remove what was clearly reconstructed badly, not all the bins for all classes have been fit, given that there are many of them where the events are poorly measured (mostly due to incomplete or wrong energy measurements). Moreover, even with a very high statistics simulation, some bins had not enough events, especially at lower energies.

6.2.1 Class 0 events

Let us start by checking the detector's performance for class 0, i.e. all of the tracked events. As visible in Figure 6.3, using this selection the tracked events percentage is maximized for the middle energy bins, which roughly correspond to the range 300-3000 keV.
At lower energies we don't have many tracks, since the electron's energy is too small in most cases; on the other hand at higher energy, due to the Silicon's Compton cross section getting smaller, we have less tracked events[1]. Instead, the overall dependence on the zenith angle is rather weak.

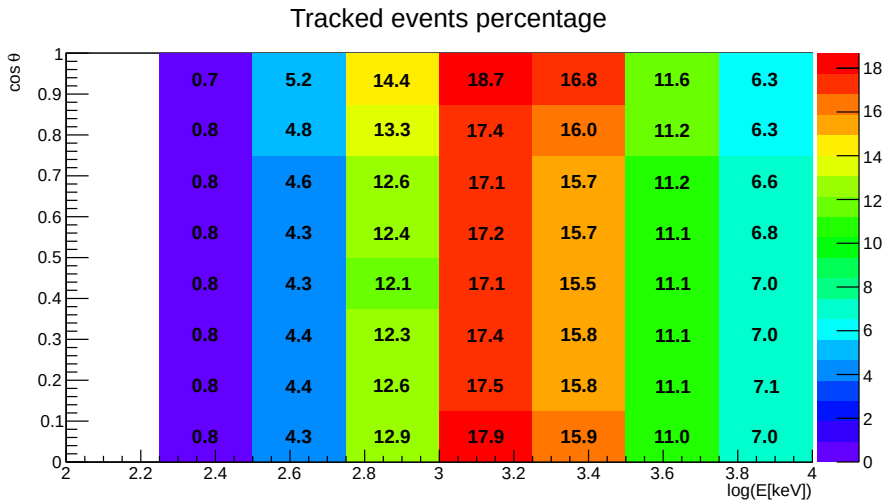

Figure 6.3: Fraction of tracked events with respect to each bin total triggered events.

In the following analysis, uncertianties have not been computed, since there are only statistical ones at this point of the design. Hence, as we cannot estimate the systematics of a more advanced design, as we did not choose the electronics design, overall uncertainties are not reliable.

The corresponding energy resolution can be seen in Figure 6.4, which is mostly dependent only upon the energy, improving as it increases.

[1]This is mainly due to the fact that, at high energy, most of the triggered events are due to the bottom calorimeter-lateral calorimeter trigger. Note, however, that at higher energies, the reconstruction sequence can classify the events wrongly, "confusing" pair events for Compton ones. This contamination becomes increasingly important as the energy increases.

This however, should not deceive us, since at energies above a few MeV, the incomplete absorption of the photons becomes a really important issue, with the full absorption peak consisting of only a small fraction of the total events, thus preventing us to fit such bins. At lower energy (log E $<$ 2.5 or E $\lesssim$ 300 keV) we have very poor statistics and such bins were thus excluded from the computation. This however, does not pose a problem, since the optimization procedure prioritizes the zone around 1 MeV. For a basic idea of the detector's performance at lower energies, see the previous section 5.2.

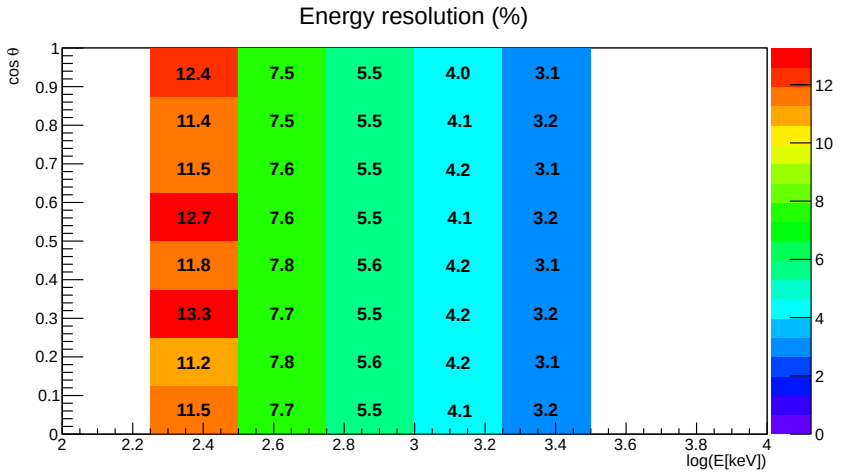

Figure 6.4: Energy resolution for tracked events.

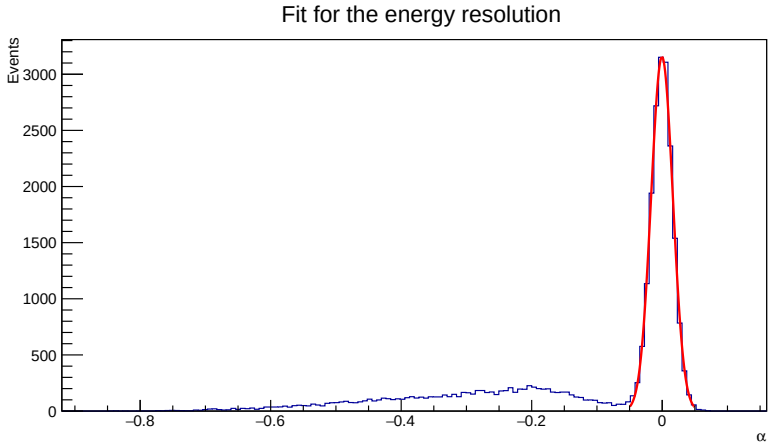

Figure 6.5: Fit for the energy resolution.

In Figure 6.5, we can see how the fit was executed for each bin. By defining the adimensional variable $\alpha = (E_{meas} - E_{sim})/E_{sim}$, where E_{meas} is the measured energy and E_{sim} the simulated one, we can just fit the full absorption peak and obtain the FWHM, which is an estimate of the energy resolution. As a last note, the energy resolution dependence on the particular class of events considered is really small, with differences of the order of $\sim$0.1%, thus the plots for the other classes will not be shown.

More interesting are the ARM and SPD dependences on energy and zenith angle, which are instead more reliant on the class selected. In Figure 6.6 we can see the ARM values behavior, which changes much more significantly with the zenith angle than with energy. The angular resolution is better at higher inclination than at normal incidence, since the greater overall thickness of the calorimeter (bottom plus lateral) allows a better measurement of the deposited energy.

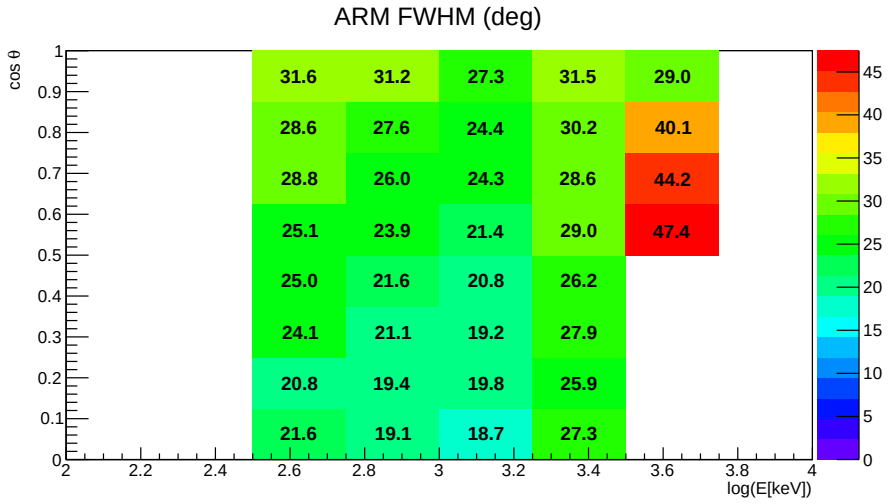

Figure 6.6: ARM for tracked events.

Fitting the ARM is slightly more complicated than the case of the energy resolution, since the peak shape is not that of any single simple distribution. The easiest approach is to fit each half of the peak with a different gauss distribution, such as showed in figure Figure 6.7. From the two fitted functions, we can then compute the FWHM of the peak. Note, however, that only fitting the peak of the distribution may result in some unreliable estimations, since we must remember that the "tails" in the spectra can strongly influence the real measure outcome.

To solve this we could, for example, take in account containment intervals. Here however, since we only need a rough estimation in the MeV region, we avoided the issue by only fitting sufficiently "well behaved" spectra.

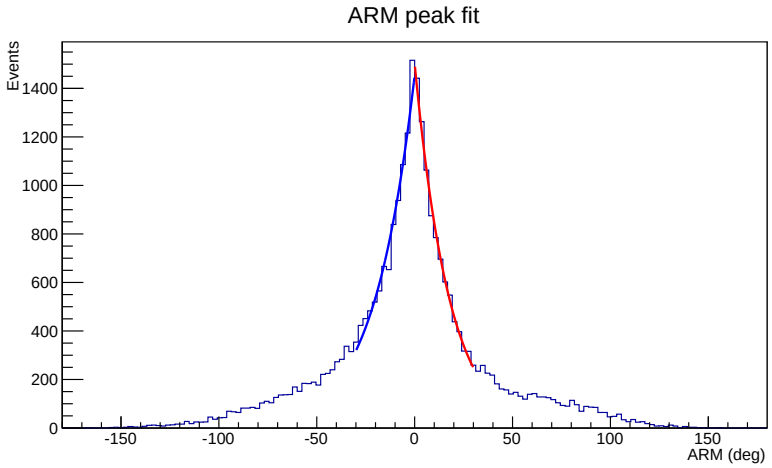

Figure 6.7: Double gaussian fit for the ARM.

The SPD half width at half maximum (HWHM) can instead be obtained by a simple gaussian fit in the first $\sim 90°$ of the spectrum, which results are visible in Figure 6.8, where we can see the SPD behavior.

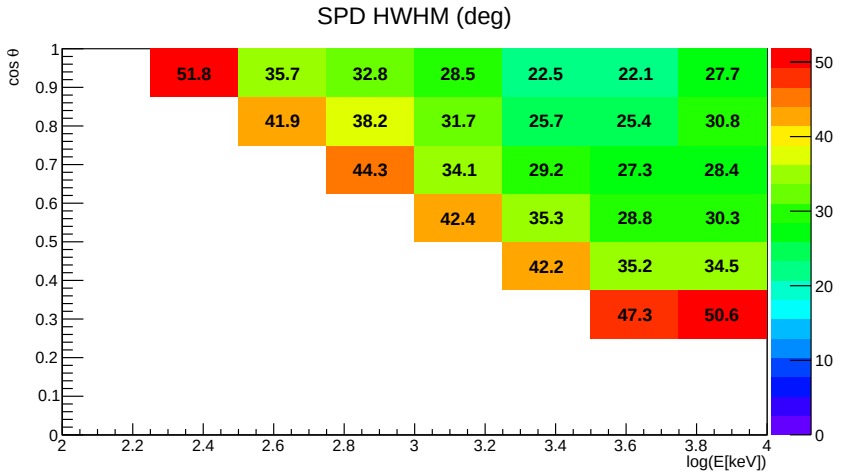

Figure 6.8: SPD for tracked events.

The missing values are due low statistics at low energy, while those at higher inclination are due the SPD spectrum getting excessively irregular and some *ad hoc* quality cut would be needed before it could be fitted. In the latter case one can conservatively assume that at this stage of the event analysis we obtain a performance very similar to untracked events (for which SPD is completely uncertain).
Finally, in Figure 6.9 we can see the effective area for the tracked events.

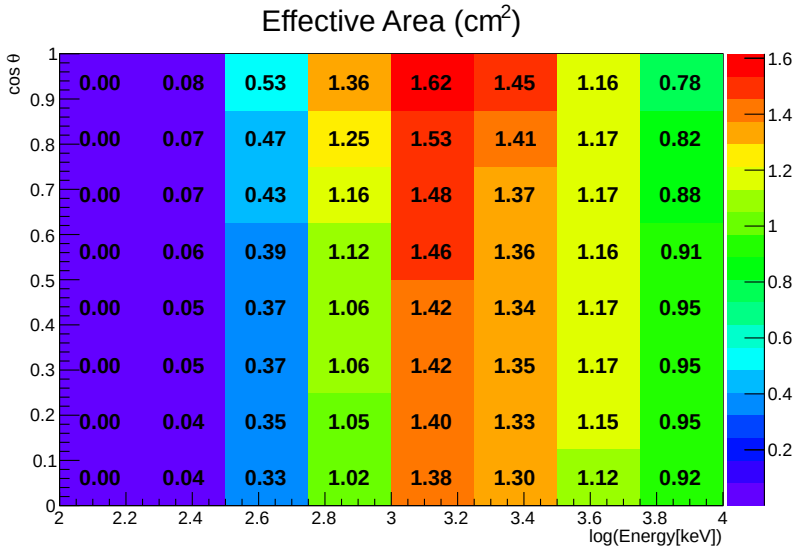

Figure 6.9: Effective area for tracked events.

The behavior of the values here mimics the one of the percentage of the tracked events, with the maximum of the effective area for values of $3 <$ log E < 3.5, which corresponds to $1 <$ E $\lesssim 3$ MeV. As we can see, the dependence on the zenith angle is rather weak, since the detector has a very large field of view in the current design.

6.2.2 Class 1 events

We can divide all tracked events according to whether they interact only in the bottom or in the lateral calorimeter. This is a kind of "geometrical" bias, since we select a part of the detector to act as a veto, however it is still interesting to see how performance changes in such a way.
Thus, selecting the tracked events without hit in the lateral calorimeter, we discard a lot of data, but obtain a far better ARM, as we can see from Figure 6.10.

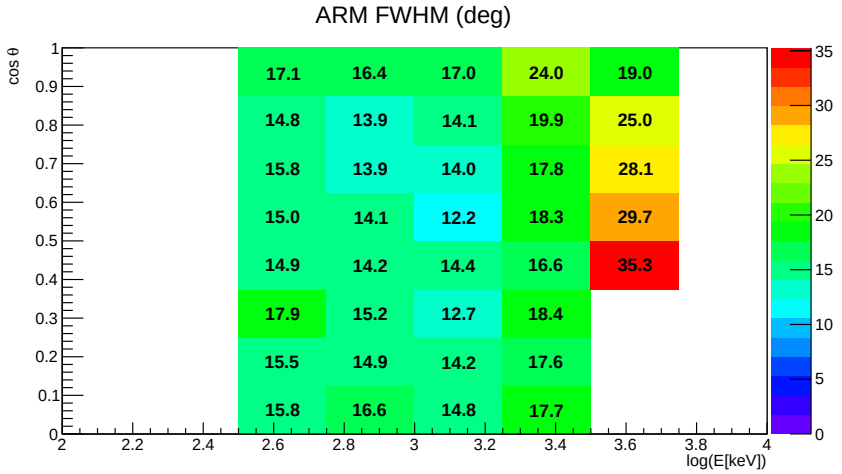

Figure 6.10: ARM for class 1 events.

The SPD, however, appears to be slightly worse than before at small angles of incidence, but it is less subject to worsening due to high zenith angles, and retains an acceptable value for a larger range, as shown in Figure 6.11.

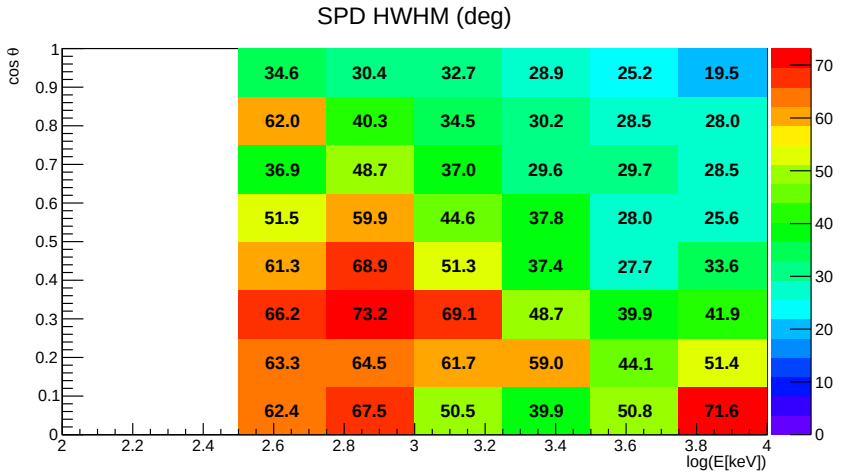

Figure 6.11: SPD for class 1 events.

From Figure 6.12, we can see that the loss of effective area is great, so, although there are improvements in the quality of the data, we are probably losing too much statistics to make use of this event class.

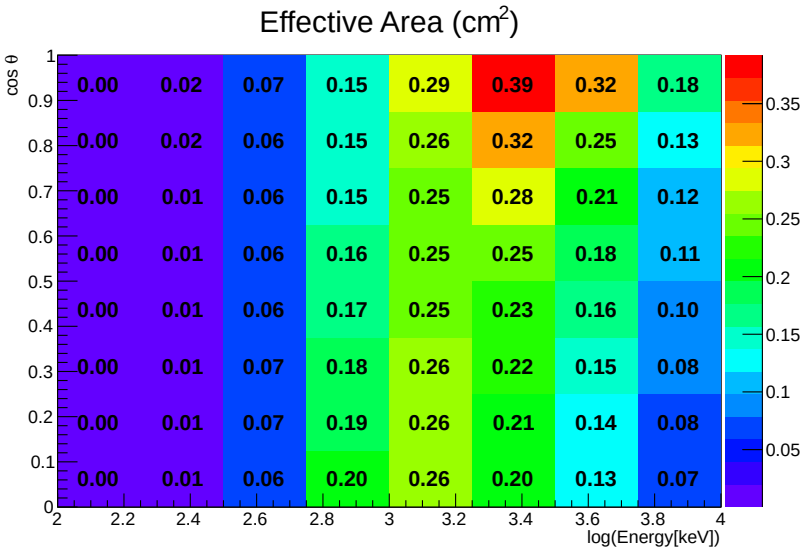

Figure 6.12: Effective area for class 1 events.

6.2.3 Class 2 events

Class 2 events are *orthogonal* to the previous one, as we now exclude the tracked events with hits in the bottom calorimeter. The amount of data is much larger in this case, however the ARM values are far worse than before, as visible in Figure 6.13.

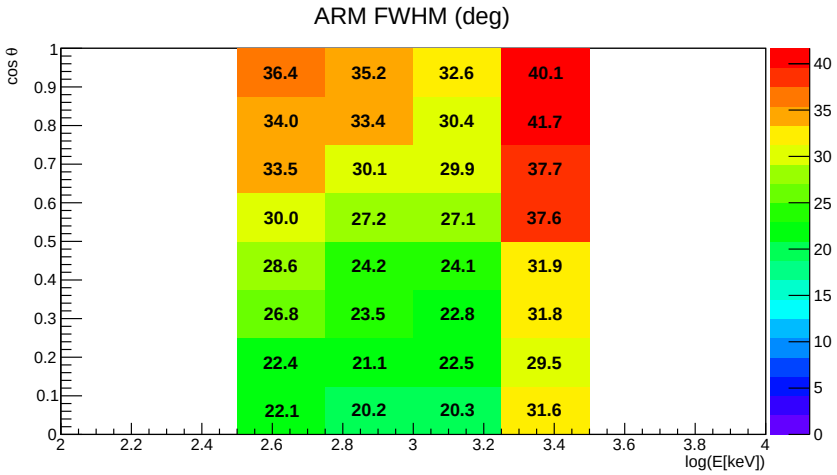

Figure 6.13: ARM for class 2 events.

For the SPD the trend is instead the opposite, as shown in Figure 6.14.

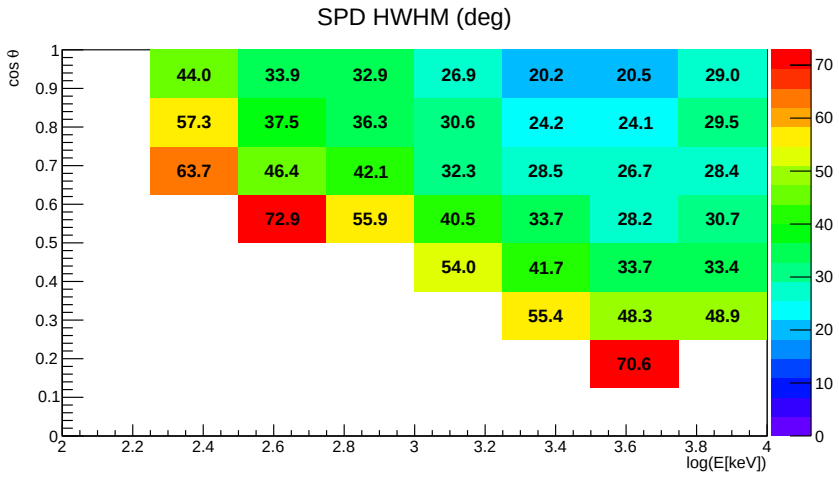

Figure 6.14: SPD for class 2 events.

Finally, in Figure 6.15, the corresponding effective area is shown.

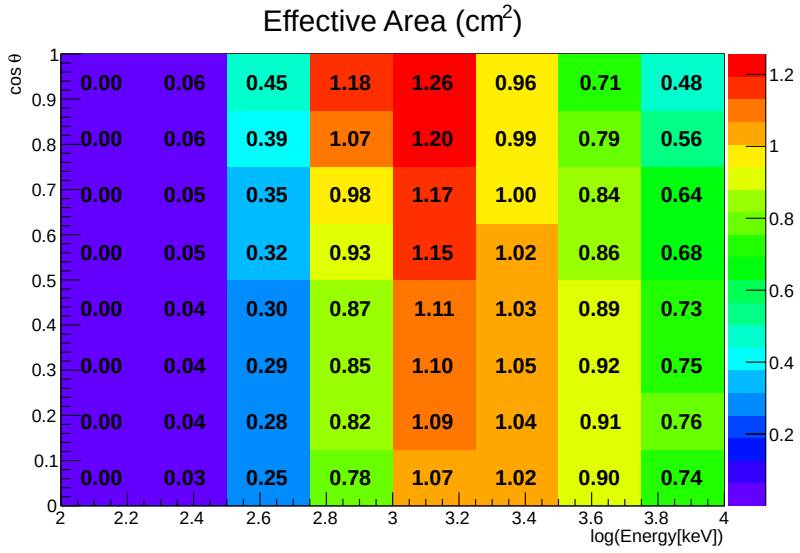

Figure 6.15: Effective area for class 2 events.

We can see that it is much greater than in the case of class 1 and gives the biggest contribution to the class 0 effective area.

6.2.4 Class 3 events

Finally, here we consider the events which have at least a hit in the tracker and in the bottom calorimeter, but none in the lateral one. As we can see from Figure 6.16, the fraction of data selected is more or less the same of the tracked events.

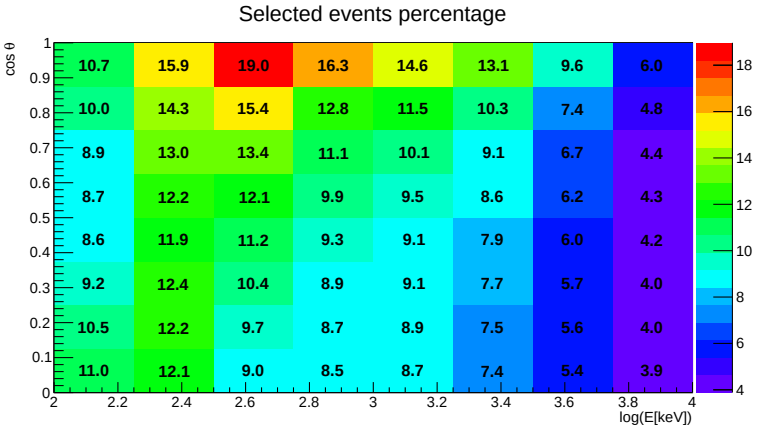

Figure 6.16: Fraction of class 3 events with respect to each bin total triggered events.

Since here we have more statistics in the lower energy bins, an estimate of their energy resolution can be computed in this case, as we can see from Figure 6.17. As visible, lower energy bins have bad resolution and are at the limits of the current detector's design capabilities.

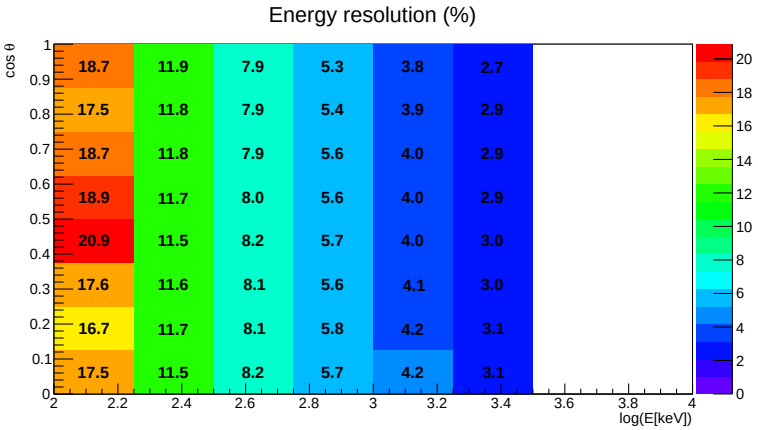

Figure 6.17: Energy resolution for class 3 events.

The same is also true for the estimated ARM values; which we can see from Figure 6.18, where the overall fit results are even better than for the tracked events.

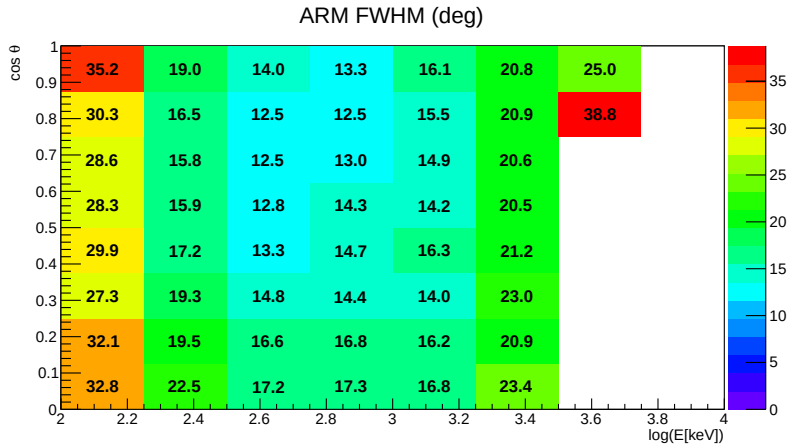

Figure 6.18: ARM for class 3 events.

Since the SPD is not defined for untracked events, as last thing we will only see the effective area values in Figure 6.19, which this time favor lower energy bins, compared to the case of the tracked events.

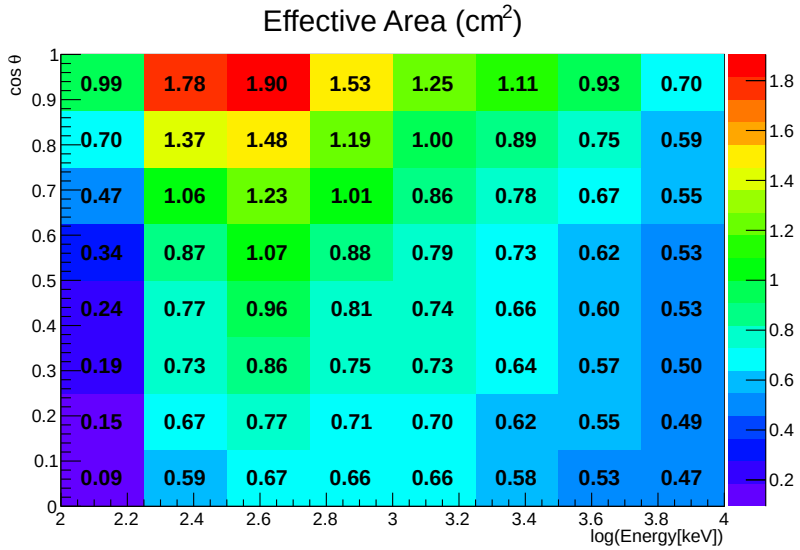

Figure 6.19: Effective area for class 3 events.

This class yields some interesting results in terms of data quality, and since it favors lower energies compared to the tracked event selection, it could be used together with tracked events in such bins[2](which are a really small fraction there).

6.3 Background

Having now a good idea of what the detector's behavior is, we can finally advance to the last part of this thesis work and start discussing the background. We will first briefly see what the main contributions are and then proceed to implement them in the simulations. Lastly, as a parameter to estimate the detector's performance in presence of background, the sensitivity will be computed.

6.3.1 Background sources

Aside from the detector's internal noise due to the electronics, which is not present in the current design, there are four main sources of background:

- **Extra-galactic gamma-ray background**: or EGB for short, is a diffuse, isotropic and homogeneous photon background. Its origin is mainly due to unresolved sources (see [11] for example), plus a possible much smaller truly diffuse component. The unresolved component is due to the PSF tails of stronger sources, or due to faint sources (flux below sensitivity).

- **Charged background**: another source of background is due to the incoming flux of charged particles (mostly protons, but also light nuclei, electrons and positrons). The are many sources of charged particles, ranging from extragalactic and galactic to the the Sun or the Earth, however the vast majority of this radiation can be effectively shielded using an anticoincidence detector, thus lowering the contribution to the same order of magnitude of the EGB[3].

[2]Note however that these two classes are partially overlapping, with roughly a third of the class 3 events actually having a track.

[3]From a rough estimation, the charged background contribute is expected to be $\sim$2·EGB.

- **Earth's albedo**: this is by far the most problematic source of background. The Earth's gamma-ray albedo is due to the interaction of the cosmic rays with the upper layers of the atmosphere. Among the other products of the reactions which take place there, there are of course gamma-rays. This implies a strongly anisotropic emission, which peaks at $\sim 113°$ with respect to the zenith of a detector pointing outwards the Earth's surface (in a LEO). Note that the albedo is by far the brightest source at the energies we are studying for our detector.

- **Activation**: due to the continuous incidence of radiation, both charged and uncharged, the detector material become progressively more radioactive, until some equilibrium between the production of new radioactive nuclei and their decays to stable isotopes is reached. This process is very difficult to evaluate, but the equilibrium would probably be obtained after several months.
  With activation, the detector has to deal with an additional internal source of background, which can generate both charged and neutral particles through the multitude of possible decays, each of them with their respective energy spectrum for the particles produced.
  This kind of background is much more relevant in a HEO then a LEO, since the Earth's magnetic field can offer some protection against the incoming charged radiation[4]. Thus, in our case this background source is negligible if compared to the Earth's albedo and it won't be further analyzed in the context of this thesis.

6.3.2 Background simulation

Regarding the more practical issue of simulating the background spectra, we do not need to simulate both source and background at the same, since we can just merge the data in the end. The simulated spectra are meant for a LEO.
The EGB and albedo spectra used for the simulations are taken from MEGAlib. In Figure 6.20 we can see the EGB energy distribution.
As you can see, the spectrum starts at $\sim$0.8 MeV, but this is not a problem, since the energy region in which we are most interested, which is around 1 MeV, is included. The EGB angular spectrum is instead isotropically distributed between $0 \leq \theta \lesssim 113°$, but not any further due to Earth absorbing the photons from behind the space telescope.

[4] In a LEO, the vast majority of charged cosmic rays hit the detector while it is in the *South Atlantic Anomaly*. The flux is strongly dependent on the particular orbit considered.

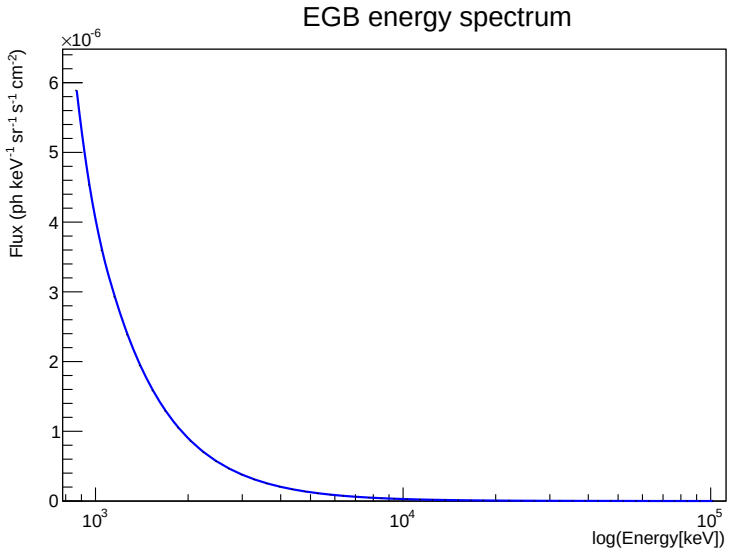

Figure 6.20: EGB energy spectrum (as simulated).

For the albedo we have a spectrum with a similar shape, in this case, however, we have a much greater overall flux ($\sim$0.036 ph/cm^2·s for the EGB compared to $\sim$0.94 ph/cm^2·s for the albedo, integrating in both solid angle and energy). In Figure 6.21 we can instead see a plot of the energy spectrum for the albedo.

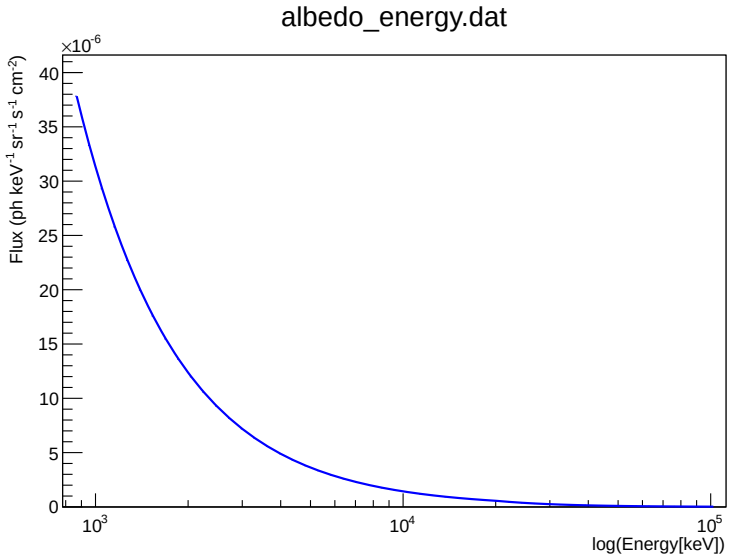

Figure 6.21: Albedo energy spectrum (as simulated).

Both the EGB and the albedo distribution could be roughly approximated by a power law of energy index -2.
In Figure 6.22 we can also see the albedo angular distribution, which is dependent on the zenith angle θ. The spectrum is comprised in the range $90° \leq \theta \leq 180°$ and peaks at $\sim 113°$, corresponding to the Earth's limb.
Notice, however, that even knowing this, there is no easy way to remove the albedo, since there is nothing to prevent the events from being triggered, or which allows us to remove them straight away during the data analysis. This was possible in COMPTEL thanks to his big dimensions, which allowed a time-of-flight measurement that is simply not possible for a CubeSat, due to its small size.

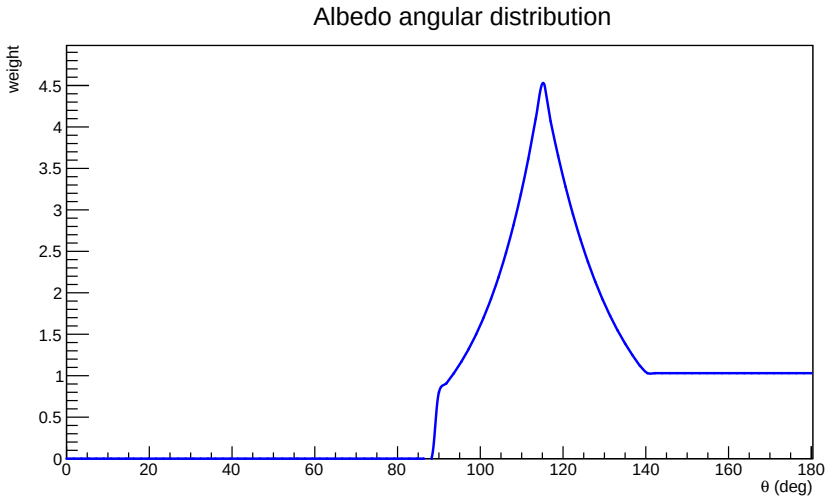

Figure 6.22: Albedo angular spectrum in function of θ zenith angle (as simulated).

The next step would be to try to find some cuts which allow us to improve the signal to background ratio. During the last part of the thesis work, a search for such cuts has been done, both manually and with TMVA's boosted decision trees, however no easily recognizable signature for the background events was found. In fact, aside from some minor cuts, no clear distinction emerged from the comparison of the background spectrum (in particular the albedo) and the source's one, as you can, for example, from Figure 6.23.

It is clear that this issue needs a deeper analysis, probably through some more advanced unsupervised method, which is beyond the scope of this thesis.

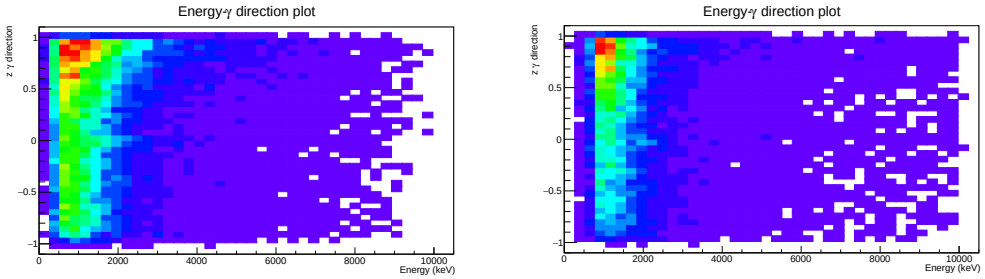

(a) Source (b) Albedo

Figure 6.23: Comparison between the energy-direction of the scattered gamma plots for tracked events of source and albedo.

6.4 Detector sensitivity

In this last part of the thesis we will see how the sensitivity of the detector was calculated, which, as explained in section 1.1, represents the ability of a detector to distinguish a weak source from the background. Physically, it is a flux, either in photons or in energy. There are more types of sensibilities involved for a Compton detector:

- **Continuum sensitivity**: the sensitivity needed to distinguish a source's continuous energy spectrum from the background.
- **Line sensitivity**: the same as the continuum sensitivity, except for the fact the this time the search for a source's flux is restricted to a specific energy line, which allows a far better background removal compared to the previous case.
- **Polarization sensitivity**: ability of the detector to measure the polarization of a source (if the source emits polarized radiation).

For most astrophysical sources, the continuum sensitivity is the one of most interest, and was thus the only one calculated (using Poisson's statistics) following the same principles explained in section 1.1:

$$F_{ph} = \frac{z\sqrt{N_{src} + N_{bkg}}}{T_{eff}A_{eff}} \tag{6.2}$$

where N_{src} is the number of source photons, N_{bkg} is the number of background photons, T_{eff} is the effective observation time[5], A_{eff} is the effective area[6] for the detector and z the statistical significance desired for the source (i.e. the number of Poisson's error bars, usually $z = 3$ or $z = 5$).
The simulation for the source is a power law with energy index -1, as defined in section 6.1, but this time it's only at normal incidence ($\phi = 0, \theta = 0$), since we only wish to have a rough estimate of the detector's sensitivity to compare to COMPTEL's one. It was then decided to restrict the computation to the most performing bin of the tracked events of the simulation, which is the one with normal incidence with energy 3.0< log E <3.25 (1.0<E$\lesssim$1.78 MeV). For the same reason, for now we neglect choosing a specific orbit and computing viewing angles and occultation times.

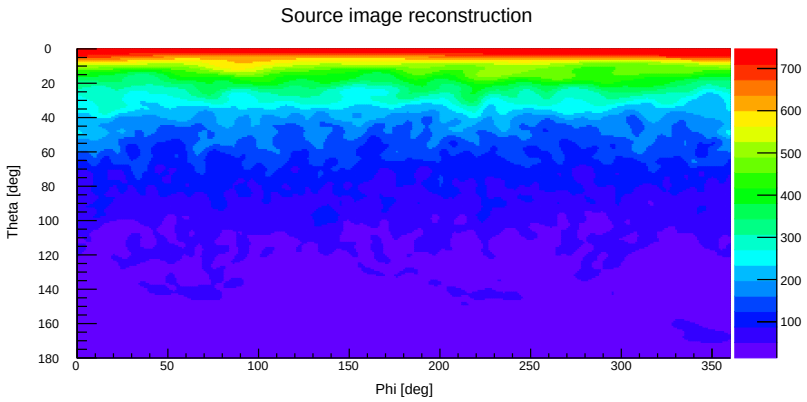

Figure 6.24: Source image reconstruction.

The source's simulation has high statistics, with a flux much higher than the sensitivity. This is to obtain a "smooth" reconstructed spectrum (see Figure 6.24), as to remove any possibility that the results depend on statistical fluctuation. The image reconstruction, which is done through Mimrec, shows the distribution of the source counts per unit of solid angle, although the normalization used here is arbitrary.

[5] T_{eff} is the time the source spends in the detector field of view minus the dead time, which here we did not consider. In survey mode, we can expect the source to spend roughly half of the real time in the space telescope field of view.

[6] Note that A_{eff} is dependent on the zenith angle, which means that, in the realistic case of an orbiting space telescope, the effective area must be averaged on the time spent at each zenith angle.

Since we are at least sure that any source has zenith angle $\theta \leq 90°$, we will discard events with $\theta > 90°$ for all the spectra.
For the EGB and the albedo, we can similarly generate a spectrum, which can be scaled up or down (i.e. more or less observation time) as long as the distribution has enough statistics to do that properly.

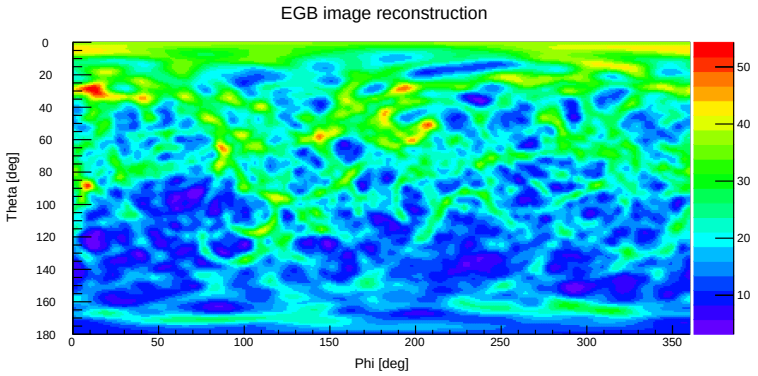

Figure 6.25: EGB image reconstruction.

In Figure 6.25 we can see the EGB image reconstruction, while in Figure 6.26 the albedo is visible, both have the same observation time. Notice how the two have opposite zenith angle event distribution, since the albedo is emitted by the Earth, which at the same time obscures the EGB. Again, most of the albedo is correctly discarded as coming from below, but a fraction contaminates the field of view

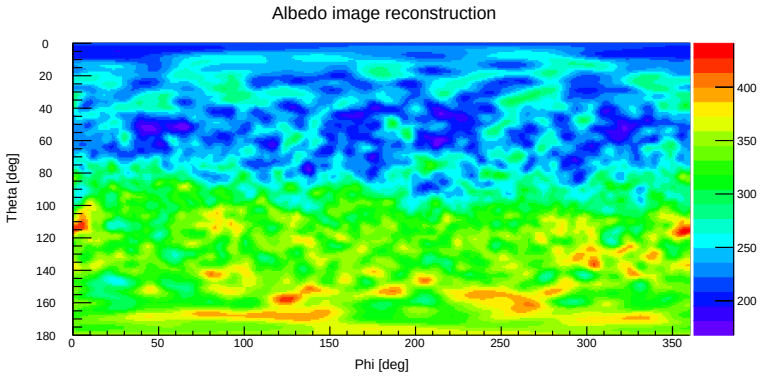

Figure 6.26: Albedo image reconstruction.

Since all of the spectra can be opportunely rescaled to a different observation time, we can use that to find the 3σ sensitivity for an observation time of 10^6 s (much bigger that what actually simulated), which we can directly compare to the one in Figure 1.6. To compute the sensitivity we just need to rescale the counts for source and background, since T_{eff} and A_{eff}(=1.62 cm^2 from Figure 6.3) are fixed parameters here.
N_{bkg} is given by the sum of N_{egb}, N_{alb}, N_{chg}, which are respectively the contribution due to EGB, albedo and charged background. As stated before, $N_{chg} \simeq 2N_{egb}$, while a quick comparison between EGB and albedo events in the bin of interest yields $N_{alb} \simeq 15N_{egb}$. It is then clear that the albedo is by far the main background contribution for our detector.

To roughly estimate the photon sensitivity, all we need to do is compare the source and background events for $0° \leq \theta \leq 90°$, since we need to find the statistical significance of the relative excess of counts caused by the presence of the source's flux.
Thus, calculating the measured events for $T_{eff} = 10^6$ s, we find $N_{alb} \simeq 1.0{\cdot}10^5$ and $N_{egb} \simeq 9.4 \cdot 10^3$, which roughly corresponds to a total background of $N_{bkg} \simeq 1.3{\cdot}10^5$ events; while for the simulated source we have $N_{src} \simeq 1.3{\cdot}10^3$. Since $N_{src} \ll N_{bkg}$, the corresponding statistical significance is given by:

$$z = \frac{N_{src}}{\sqrt{N_{bkg} + N_{src}}} \simeq \frac{N_{src}}{\sqrt{N_{bkg}}} \tag{6.3}$$

and we find $z \simeq 3.7$.

If we want the 3σ sensitivity, we just need to rescale the original source's total count (all of the sky) $N_{src}^{tot} \simeq 1.7 \cdot 10^3$ by the quantity $3/z$, and we find that this corresponds to a sensitivity (in photon flux) of:

$$F_{ph} = \frac{N_{src}^{tot}}{T_{eff} A_{eff}} \cdot \frac{3}{z} \tag{6.4}$$

which yields $F_{ph} \simeq 8.5{\cdot}10^{-4}$ ph/cm^2·s, however this is not yet what we desire, since we need the energy flux to be able to compare our value to COMPTEL's one. To do that, we can just multiply the sensitivity in photons by the average value of the energy in the bin, which is given by:

$$\overline{E} = \frac{\int_{E_{min}}^{E_{max}} E \cdot \frac{dN}{dE} \mathrm{d}E}{\int_{E_{min}}^{E_{max}} \frac{dN}{dE} \mathrm{d}E} = \frac{\int_{E_{min}}^{E_{max}} E \cdot AE^{-1} \mathrm{d}E}{\int_{E_{min}}^{E_{max}} AE^{-1} \mathrm{d}E} = \frac{E_{max} - E_{min}}{\log E_{max} - \log E_{min}} \tag{6.5}$$

where, with reference to Equation 6.1, $A = N_0 E_0$, since we are using a power law with energy index -1, and E_{max}=1.78 MeV, while E_{min}=1.00 MeV. The calculation yields $\overline{E} = 1.35$ MeV, hence the final sensitivity value is $F_E = F_{ph}\overline{E} = 1.2 \cdot 10^{-3}$ MeV/cm^2·s. Again, here no uncertainty is given due to the unfinalized nature of the current design, as the electronics has not been selected yet and the unknown contributions of the systematics would only yield a very unreliable value for the uncertainties.

In such a way we obtained a very rough estimate of the sensitivity of our detector, which, as we can see from Figure 1.6, is still not as good as the value from COMPTEL in the same conditions, which roughly is $F_E \sim 2 \cdot 10^{-4}$ MeV/cm^2·s. It must be noted, however, that for our calculation only very minor cuts have been applied, hence, if better cuts were to be found, the sensitivity value would improve dramatically (see next chapter).

7 Next steps

Through this thesis the concept of the detector was improved from a very simplistic design, starting basically from zero, to an improved (but not finished) design, with a rough estimation of the expected performance. This, of course, does not conclude the work which needs to be done, but builds a solid foundation from which further studies can proceed. In particular, it is clear that the viability of the design is strongly dependent on ability to remove at least a good part of the background, since we wish to reach a better sensitivity compared to COMPTEL's one. The biggest issue here is the albedo, which removal should be the top priority for the future of the detector. There are only two ways to solve this issue:

- Blocking the albedo photons via material shielding: using for example a lead shield. This, however, would not be a viable solution for a CubeSat. For example, if we wanted to shield 90% of the photons at $\sim$1 MeV from the rear of the space telescope, we would need a lead shield $\sim$2.9 cm thick, which would imply an excessive weight. A viable solution is instead to place the CubeSat on the *International Space Station*, which would act as shield against the albedo photons (e.g. exposed platforms exist that can host small experiments and detectors, effectively shielding the payload from the Earth emission below).

- Removal of albedo events via data analysis: finding opportune cuts, it may be possible to strongly decrease the background events. However, since the signature for albedo events is not easy to find, if there is a signature at all, the is no guarantee that this is feasible, although it must be said that removing even only half of the albedo events would greatly improve the sensitivity, and this without the need to add any kind of shielding to the detector. It would also be a great improvement if we are able to reject at least part of the albedo at the trigger level (i.e. the trigger does not activate for the albedo events), since it would reduce the dead time of the detector and the quantity of data which needs to be filtered.

In particular, it is interesting to make a rough prediction of how much the detector's sensitivity would improve as we reduce the albedo background contributions. As explained in section 6.4, $N_{bkg} = N_{egb} + N_{alb} + N_{chg}$, with approximately $N_{chg} \simeq 2N_{egb}$ and $N_{alb} \simeq 15N_{egb}$. Thus, if we decrease only the albedo and keep the other parameters fixed, the sensitivity changes as indicated by Table 7.1.

Albedo (N_{egb})	Sensitivity (MeV/cm^2·s)
15	$1.2{\cdot}10^{-3}$
10	$1.0{\cdot}10^{-3}$
5	$8.0{\cdot}10^{-4}$
2	$6.6{\cdot}10^{-4}$

Table 7.1: Sensitivity improvement with albedo reduction.

As we can see, reducing the albedo greatly improves the sensitivity, although that alone will not be enough to achieve COMPTEL's sensitivity, at least not if we use only tracked events.
However, if we can achieve such value, then it would be surely worth to proceed with the design, adding the electronics and the read-outs, thus finally introducing their noise contribution to the detector. After that, it would be possible to enter a more advanced stage of simulation, where more precise predictions on the detector's performance could be made. In particular, improving the angular resolution with a dedicated analysis would further boost the sensitivity, making it possible to reach the COMPTEL level. Furthermore, being the detector small and relatively simple, all of this work could still be done rather quickly, and the space telescope could be launched within a short time, obtaining the important data in the medium energy range which gamma-ray astronomy needs nowadays.

Bibliography

[1] M. Ajello at al. A. A. Abdo, M. Ackermann. Fermi LAT observations of Markarian 421: the missing piece of its spectral energy distribution. *Astrophysical journal*, 2011.

[2] R. Andritschke A. Zoglauer and F. Schopper. *MEGAlib - The Medium Energy Gamma-ray Astronomy Library*, 2005.

[3] A.A. Moiseev at al. Compton-pair production space telescope (ComPair) for MeV gamma-ray astronomy. 2015.

[4] M. Tavani at al. ASTROGAM: Summary of a proposal submitted for the ESA M4 mission programme. 2015.

[5] W.B Atwood at al. The Large Area Telescope on the Fermi gamma-ray space telescope mission. 2009.

[6] Pietro Ubertini Jörn Wilms Christoph Winkler, Roland Diehl. INTEGRAL: science highlights and future prospects.

[7] A. Zoglauer et al. *MEGAlib - Simulation and Data Analysis for Low-to-medium-energy Gamma-ray Telescopes.*

[8] Schonfelder et al. Instrument description and performance of the imaging gamma-ray telescope COMPTEL aboard the Compton gamma-ray observatory. *The astrophysical journal supplement series.*

[9] Stacy et al. The response of CGRO COMPTEL determined from Monte Carlo simulation studies. *Astronomy and astrophysics supplement series.*

[10] Giulio Lucchetta. Design and optimization around 1 MeV of a tracker for a CubeSat mission, 2016.

[11] D. Gasparrini et al. M. Ajello. The origin of the extragalactic gamma-ray background and implications for dark-matter annihilation. 2015.

[12] C. Megan Urry and Paolo Padovani. Unified schemes for radio-loud active galactic nuclei. 1995.

[13] Andreas Christian Zoglauer. *First Light for the Next Generation of Compton and Pair Telescopes*. PhD thesis, Max-Planck-Institut für extraterrestrische Physik, 2005.